HHS Public Access

Author manuscript

Nature. Author manuscript; available in PMC 2025 April 01.

Published in final edited form as:

Nature. 2024 April ; 628(8006): 162–170. doi:10.1038/s41586-024-07238-x.

Depleting myeloid-biased hematopoietic stem cells rejuvenates aged immunity

Jason B. Ross[1,2,3,*], **Lara M. Myers**[4,*], **Joseph J. Noh**[1,2], **Madison M. Collins**[4,6], **Aaron B. Carmody**[5], **Ronald J. Messer**[4], **Erica Dhuey**[1,2], **Kim J. Hasenkrug**[4,#], **Irving L. Weissman**[1,2,#]

[1]Institute for Stem Cell Biology and Regenerative Medicine, Stanford University School of Medicine, Stanford, CA, USA.

[2]Ludwig Center for Cancer Stem Cell Research and Medicine, Stanford University School of Medicine, Stanford, CA, USA.

[3]Department of Radiation Oncology, Stanford University School of Medicine, Stanford, CA, USA.

[4]Laboratory of Persistent Viral Diseases, Rocky Mountain Laboratories, National Institutes of Allergy and Infectious Diseases, National Institutes of Health, Hamilton, MT, USA.

[5]Research Technologies Branch, Rocky Mountain Laboratories, National Institutes of Allergy and Infectious Diseases, National Institutes of Health, Hamilton, MT, USA.

[6]Present address: Department of Biological and Physical Sciences, Montana State University Billings, Billings, MT, USA.

Abstract

Aging of the immune system is characterized by decreased lymphopoiesis and adaptive immunity, and increased inflammation and myeloid pathologies[1,2]. Age-related changes in populations of self-renewing hematopoietic stem cells (HSCs) are thought to underlie these phenomena[3]. During youth, HSCs with balanced output of lymphoid and myeloid cells (bal-HSCs) predominate over HSCs with myeloid-biased output (my-HSCs), thereby promoting the lymphopoiesis required for initiating adaptive immune responses, while limiting the production of myeloid cells, which can be pro-inflammatory[4]. Aging is associated with increased proportions of myeloid-biased HSCs

Correspondence to: Irving L. Weissman, Institute for Stem Cell Biology and Regenerative Medicine, Ludwig Center for Cancer Stem Cell Research and Medicine, Stanford University School of Medicine, Stanford, CA, 94305, USA, irv@stanford.edu; Kim J. Hasenkrug, Laboratory of Persistent Viral Diseases, Rocky Mountain Laboratories, National Institutes of Allergy and Infectious Diseases, National Institutes of Health, Hamilton, MT, 59840, USA, khasenkrug@nih.gov.

*These authors contributed equally to this work.

#Hasenkrug and Weissman are co-senior authors

Author Contributions

J.B.R. and L.M.M. contributed equally to this work and either has the right to be listed first in bibliographic documents. J.B.R. and L.M.M. conceived and performed experiments, analyzed and interpreted all the data, and wrote the paper. J.J.N, M.M.C., A.B.C, R.J.M, and E.D. performed experiments and analyzed data. L.M.M., M.M.C., A.B.C, and R.J.M performed the Friend Virus experiments. J.B.R and E.D. designed and performed the RNA-seq and transplant experiments. I.L.W. and K.J.H. conceived experiments, supervised the research, interpreted results, and wrote the paper. All authors reviewed, edited, and approved the manuscript.

Competing Interest

The authors declare the following competing interests: I.L.W. is an inventor on patents related to CD47 licensed to Gilead Sciences, Inc, but has no financial interests in Gilead. He is also a co-founder and equity holder of Bitterroot Bio, Inc., PHeast Inc, and 48 Bio. He is on the SAB of Appia, Inc. J.B.R is a co-founder and equity holder of 48 Bio. I.L.W, K.J.H., J.B.R., L.M.M., and J.N.N. are co-inventors on a pending patent application related to this work. The remaining authors declare no competing interests.

resulting in decreased lymphopoiesis and increased myelopoiesis[3,5,6]. Transfer of bal-HSCs results in abundant lymphoid and myeloid cells, a stable phenotype retained with secondary transfer; my-HSCs also retain their patterns of production on secondary transfer[5]. The origin and potential interconversion of these two subsets is still unclear. If they are separate subsets postnatally, it might be possible to reverse the aging phenotype by eliminating my-HSCs in aged mice. Here we demonstrate that antibody-mediated depletion of myeloid-biased HSCs in aged mice restores characteristic features of a more youthful immune system, including increasing common lymphocyte progenitors (CLPs), naïve T cells, and B cells, while decreasing age-related markers of immune decline. Depletion of my-HSCs in aged mice improves primary and secondary adaptive immune responses to viral infection. These findings may have relevance to understanding and intervening with diseases exacerbated or caused by dominance of the hematopoietic system by my-HSC.

Main

A single hematopoietic stem cell (HSC) can generate all blood cells and self-renew to maintain the stem cell pool throughout life[2]. HSCs demonstrate functional heterogeneity and can differ in their contribution to the lymphoid and myeloid cell lineages[7-9]. At least two HSC subsets exist: (i) balanced HSCs (bal-HSC) that provide balanced production of lymphoid and myeloid cells, and (ii) myeloid-biased HSCs (my-HSC) that are biased towards predominant production of myeloid cells[3,5,10]. The frequency of my-HSCs relative to bal-HSCs increases with age[1,11]. This age-related shift from bal-HSCs to my-HSCs decreases lymphopoiesis and increases myelopoiesis[12], thereby contributing to numerous pathologies of the elderly, including reduced adaptive immunity[13], 'inflammaging'[14], and several myeloid-related diseases. To address these and other age-related pathologies, we sought to develop a therapy to return the immune system to a more youthful state characterized by less myeloid-biased HSCs and more HSCs with balanced production of lymphoid and myeloid lineage cells.

To test whether antibody-mediated depletion of my-HSCs might enable bal-HSCs to reverse age-related immune decline by restoring lymphopoiesis and limiting myeloid cell-driven inflammation, we identified distinct cell-surface markers on my-HSCs compared to bal-HSCs[5,15-20], targeted and depleted my-HSCs *in vivo,* and characterized the impact of their depletion on the hematopoietic system and immune phenotypes, including functional immunity to new infections.

Identifying surface antigens on my-HSCs

To identify candidate targets for therapeutic depletion of my-HSCs, we first established and validated a set of cell-surface antigens on my-HSCs (Fig. 1a-c, Extended Data Fig. 2a). Mouse HSCs ($Lin^{-}cKIT^{+}Sca1^{+}FLT3^{-}CD34^{-}CD150^{+}$)[15] can be separated into my-HSCs or bal-HSCs based on their expression levels of CD150 (*Slamf1*); my-HSCs are $CD150^{High}$, while bal-HSCs are $CD150^{Low}$ [5,16]. In addition to CD150, several markers of HSCs with myeloid bias have been described[18,19]. To identify the best target to deplete my-HSCs, we conducted a systematic search of all potential antigens increased relatively or absolutely on

my-HSCs. My-HSCs are more abundant in aged animals[5] and in subpopulations of HSCs defined by a combination of markers and/or genetic reporters[19,21,22]. Thus, we reasoned that my-HSC specific genes would be enriched in transcriptional datasets of (i) HSCs from aged animals[23-31], and (ii) HSCs with functional myeloid-bias[19,21,22] (Fig. 1a). Examination of these datasets yielded 12 candidate genes encoding cell-surface proteins that were highly enriched in aged and/or myeloid-biased HSCs (Fig. 1a, Extended Data Fig. 2a). As expected, CD150 emerged from this analysis, along with several markers associated with myeloid-biased HSCs: CD41[17], CD61[18], CD62p[20], and NEO1[19]. To validate these candidates and identify the best target on my-HSCs, we evaluated their cell-surface levels on my-HSCs and bal-HSCs with antibodies and flow-cytometry.

Since the ideal target antigen to deplete my-HSCs would be highly expressed on the cell-surface of my-HSCs relative to bal-HSCs, we compared the cell-surface expression of each candidate antigen on my-HSCs and bal-HSCs using marker-specific antibodies (Fig. 1b). For each marker, the fold-enrichment was calculated for my-HSCs based on the proportion of my-HSCs ($CD150^{High}$ HSCs) relative to bal-HSCs ($CD150^{Low}$ HSCs) that were marker-positive. Antibodies to NEO1 and CD41 resulted in a significantly increased frequency of staining of my-HSCs (Fig. 1b, 1e), consistent with NEO1 and CD41 marking HSCs with myeloid bias[17,19]. Among the remaining candidates, CD62p led to the greatest enrichment for my-HSCs (Fig. 1b-e). Overall, the most highly enriched cell-surface proteins on my-HSCs relative to bal-HSCs were CD41, CD62p, and NEO1 (Fig. 1b-c). Together with CD150, we focused on these cell-surface proteins as candidate target antigens for antibody-mediated depletion of my-HSCs.

To provide insight into potential off-target effects from antibody treatment, we determined the expression of each candidate on hematopoietic progenitor cells (HPCs) and mature differentiated cells, as well as non-hematopoietic tissues. HSCs generate multi-potent progenitors (MPPs), which generate lineage-restricted common myeloid progenitors (CMPs) [32] and common lymphoid progenitors (CLPs) [33]. Flow-cytometry revealed that none of the candidate surface proteins were highly expressed by these subsets, other than CD41, which was abundantly expressed in megakaryocyte progenitors (MkPs) (Fig. 1f-h, Extended Data Fig. 2b-h). These results were largely concordant with transcriptomic profiling of these same sorted populations from independent datasets (Extended Data Fig. 1a-l) [31]. The most promising candidates – CD150, CD41, CD62p, NEO1 – were not highly expressed in mature hematopoietic cells by RNA (Extended Data Fig. 1m) or by flow-cytometry (Extended Data Fig. 2g-h) and were relatively specific to the hematopoietic system compared to other tissues (Extended Data Fig. 1n-o). These results demonstrated the relative specificity of these markers to my-HSCs compared to bal-HSCs, hematopoietic progenitors and mature cells, and non-hematopoietic tissues.

Given the increased abundance of my-HSCs with age[3,5], we evaluated if HSCs isolated from aged mice demonstrated increased expression of the candidate markers we identified. We evaluated HSCs in mice spanning approximately six months to one year of age, focusing on CD41, CD62p, and NEO1, which were the most highly enriched markers on my-HSCs. We observed a significant positive correlation with the proportion of my-HSCs and mouse age, consistent with the expansion of my-HSCs during aging[5] (Fig. 1i, Extended Data Fig. 2j).

Similarly, we also observed a strong positive correlation with age and the percentage of total HSCs that were NEO1$^+$, CD41$^+$, or CD62p$^+$ (Fig. 1j-k, Extended Data Fig. 2i), consistent with NEO1, CD41, and CD62p marking my-HSCs that increase with age. We selected these cell-surface antigens, along with CD150, as candidate targets to deplete my-HSCs *in vivo*.

Antibody-mediated depletion of my-HSCs

We next determined if we could deplete my-HSCs *in vivo* by targeting these my-HSC antigens (Extended Data Fig. 5a). We focused on CD150, CD62p, and NEO1, which demonstrated the greatest enrichment for my-HSCs relative to bal-HSCs and HPCs (Fig. 1b-h). We developed independent antibody-conditioning regimens to deplete my-HSCs for each target, optimizing for regulators of cell clearance, including anti-phagocytic signals[34], antibody density, and isotype.

To determine the impact of targeting CD150, we tested anti-CD150 antibodies for their capacity to deplete my-HSCs *in vivo*. We administered rat IgG2b anti-CD150 antibodies to adult mice (6-7 months) and evaluated the bone marrow after approximately one week (Extended Data Fig. 5b) [35]. To control for antibody masking, whereby *in vivo* treatment with anti-CD150 antibody might prevent the detection of target cells, we identified and validated independent non-masking antibodies to CD150 (Extended Data Fig. 3a-l). Treating mice with anti-CD150 significantly depleted my-HSCs relative to bal-HSCs by both frequency (Extended Data Fig. 4a) and absolute number (Extended Data Fig. 4b, Extended Data Fig. 4r). To verify the depletion of my-HSCs, we confirmed that HSCs expressing the independent my-HSC antigen NEO1 were also depleted with anti-CD150 (Extended Data Fig. 4c). This finding and others described below rule out single antigen modulation as the mechanism for lack of CD150 in the HSC analyses but favored depletion of cells with both markers. Consistent with rat IgG2b antibodies having greater depleting activity than IgG2a in mice, treatment with rat IgG2a anti-CD150 antibodies were only modestly effective (Extended Data Fig. 4i). Collectively, these results demonstrated that antibody-targeting of CD150 was sufficient to deplete a significant fraction of my-HSCs *in vivo*.

We optimized the my-HSC depletion protocol by considering factors that limit *in vivo* cell clearance. Since antibody-mediated depletion can be limited by the anti-phagocytic signal CD47[34,36], we speculated that blocking CD47 could enhance the depletion of my-HSCs. Compared to anti-CD150 alone, dual treatment with anti-CD150 and anti-CD47 decreased the frequency of my-HSCs relative to bal-HSCs (Extended Data Fig. 4a-b). To further decrease the threshold for cell-clearance, we added low-doses of anti-cKIT, which also depleted my-HSCs relative to bal-HSCs in the presence of anti-CD150 (Extended Data Fig. 4a-b). The addition of anti-CD47 and/or anti-cKIT to anti-CD150 increased the frequency and absolute number of bal-HSCs in the bone-marrow after approximately one week (Extended Data Fig. 4a-b), consistent with their expansion and/or redistribution after my-HSC depletion. Overall, the most effective regimen to deplete my-HSCs relative to bal-HSCs was combining antibodies to CD150, CD47, and cKIT (Extended Data Fig. 4a-b, Fig. 2a, 2d).

The optimized protocol we developed to deplete my-HSCs by targeting CD150 informed our strategy to deplete my-HSCs by targeting CD62p or NEO1. To target CD62p, we used an anti-CD62p antibody of mouse IgG2a isotype, which was predicted to have high depleting activity in mice. Indeed, administration of anti-CD62p in combination with anti-cKIT and anti-CD47 significantly depleted my-HSCs in the bone-marrow after approximately one week (Fig. 2b, 2e). To target NEO1, we combined goat anti-mouse NEO1 antisera with anti-CD47 and anti-cKIT, which also resulted in effective depletion of my-HSC in the bone marrow after approximately one week (Fig. 2c, 2f, Extended Data Fig. 5a-q). Similar to treatment with anti-CD150 (Extended Data Fig. 4c-d), treatment with anti-CD62p or anti-NEO1 also depleted HSCs expressing the my-HSC antigen NEO1 (Extended Data Fig. 4p-q). Taken together, these experiments established three separate antibody-conditioning regimens that deplete my-HSCs bearing two independent cell surface antigens *in vivo*. Again, depletion of cells marked by two independent surface antigens with antibodies to one marker only rules out antigenic modulation and favors my-HSC cellular depletions.

To verify changes in HSC composition after my-HSC depletion, we conducted gene expression profiling of purified total HSCs (KLS FLT3$^-$CD34$^-$CD150$^+$) isolated from aged (11 months) mice with or without antibody-conditioning (Fig. 2g-h, Extended Data Fig. 3m-n, 4x). Gene Set Enrichment Analysis (GSEA) revealed that HSCs isolated from mice receiving antibody-conditioning were enriched in gene-signatures of young HSCs and bal-HSCs (Fig. 2g-h), and were depleted in gene-signatures of old HSCs and my-HSCs (Fig. 2g-h, Supplementary Table 1) [18-20,22,26-29,37]. Thus, in addition to depleting HSCs marked by validated my-HSC cell-surface proteins, antibody conditioning altered the molecular composition of the HSC compartment by selectively depleting the my-HSC RNA ‘fingerprint’ cells and retaining or expanding the young or bal-HSC RNA fingerprints.

To functionally validate that changes in HSC potential are altered after antibody-conditioning, we performed transplant experiments with purified HSCs and evaluated myeloid versus lymphoid lineage potential in recipient animals. We purified 100 total HSCs (KLS FLT3$^-$CD34$^-$CD150$^+$) isolated from CD45.2 aged (11 months) mice with or without antibody-conditioning and transplanted them into age-matched (2 months) CD45.1 congenic recipient irradiated mice (Extended Data Fig. 3m-n). Peripheral blood analysis revealed that mice reconstituted with HSCs isolated from antibody-conditioned mice demonstrated a significantly decreased myeloid-to-lymphoid cell ratio compared to mice reconstituted with HSCs isolated from control mice (Fig. 2i-k, Extended Data Fig. 4t-w), consistent with antibody-conditioning depleting my-HSCs. Taken together, these results demonstrate that antibody-conditioning depletes my-HSCs *in vivo* based on cell-surface, molecular, and functional phenotypes.

My-HSC depletion rebalances progenitors

To determine the impact of depleting my-HSCs on downstream progenitors, we examined common lymphoid progenitors (CLPs) [33] and myeloid progenitors (CMPs&GMPs, MkPs, MEPs) in the bone marrow from mice receiving each antibody-conditioning regimen (Extended Data Fig. 5a-b). Approximately one-week post-treatment, all antibody protocols significantly increased the frequency of CLPs or IL7Ra$^+$ lymphocyte precursors[33] (Fig. 2d-f,

Extended Data Fig. 4j-k). Protocols targeting CD62p or NEO1 decreased the frequency of myeloid progenitors (Fig. 2e-f, Extended Data Fig. 4l-m) and increased the ratio of lymphoid progenitors (CLPs) to myeloid progenitors (CMPs&GMPs) by up to 4-fold (Extended Data Fig. 4o). The increase in lymphoid progenitors and decrease in myeloid progenitors after my-HSC depletion in adult mice pointed to the potential of this treatment to reverse age-related immune decline.

My-HSC depletion in old mice *in vivo*

To determine if reversing the age-related shift from bal-HSCs to my-HSCs would restore cells critical for immune function and reverse age-related markers of immune decline[3,5], we compared young-adult mice (3-6 months) to aged mice (18-24 months) with or without anti-NEO1 antibody-conditioning. Analyses were conducted after approximately (i) 1-week to evaluate acute effects, or (ii) 8-weeks or 16-weeks to evaluate persistent effects, which is after the estimated clearance of antibodies[35] and non-self-renewing cells[38] (Fig. 3a). Aged mice receiving antibody-conditioning demonstrated a significant decrease in my-HSCs after approximately 1-week (Fig. 3b-c) with no significant acute impact on the frequency of mature B cells or myeloid cells (Extended Data Fig. 6h-k). Interestingly, 8-weeks after treatment the frequency of my-HSCs relative to bal-HSCs was significantly reduced (Extended Data Fig. 6a), which we confirmed by absolute numbers of cells in the total bone-marrow in an independent experiment (Extended Data Fig. 9c). Thus, antibody conditioning depleted my-HSCs in aged animals at least several months after a single administration. The impact on common lymphoid progenitors (CLPs), which are non-selfrenewing progenitors[58], was evaluated next. Compared to young-adult mice, untreated aged mice demonstrated a significant decrease in the frequency of CLPs (Fig. 3d), but antibody-conditioned, aged mice showed increased frequencies of CLPs 8-weeks and 16-weeks after treatment (Fig. 3b, 3d). These results underscored the impact of a single administration of therapy to rejuvenate the hematopoietic stem cell and progenitor compartments.

My-HSC depletion increases lymphocytes

A critical deficit of aged immune systems is the reduced generation of T and B lymphocytes capable of recognizing novel antigens[13]. Given that depletion of my-HSCs in aged mice increased lymphocyte progenitors, we sought to determine if these changes were sufficient to increase naïve T and B cells. We evaluated mice after 8-weeks, since the generation of new T and B cells from HSCs peaks between 7-11 weeks[15,19]. Although we did not observe significant differences in thymus weight (Extended Data Fig. 6l), treated mice contained all the thymic progenitor subsets associated with thymus function[39] (Extended Data Fig. 6m-n). After 8-weeks, aged mice receiving antibody-conditioning demonstrated a significant increase in the frequency (Fig. 3e) and absolute number (Extended Data Fig. 7a) of circulating naïve T cells (CD4+ and CD8+, $CD44^{-}$ $CD62L^{+}$ cells) compared to age-matched controls. To further interrogate T cell subsets, we examined central (stem) [40] memory ($CD44^{+}CD62L^{+}$) and effector memory ($CD44^{+}CD62L^{-}$) cells by canonical markers or by cluster-based analysis (Extended Data Fig. 8a-b, 7f-j). Depletion of my-HSCs was associated with slightly increased central (stem) memory (CM) T cells by absolute number

(Extended Data Fig. 7b), but the absolute number of EM (EM) T cells was not significantly impacted (Extended Data Fig. 7c). As central memory T cells are derived by expansion from activated naïve T cells specific for antigens, and transition to the $CD44^{+}CD62L^{+}$ after antigen disappears, future studies will be required to determine the CM pool to defined novel antigens before and after infection. Similar to our results for T cells, aged mice receiving antibody-conditioning also demonstrated a significant increase in the frequency (Fig. 3f) and absolute numbers (Extended Data Fig. 7d) of mature circulating B cells ($CD19^{+}B220^{+}IgM^{+}IgD^{+}$). Antibody treatment did not significantly impact the total number of circulating $CD45^{+}$ leukocytes (Extended Data Fig. 7e). These results demonstrated that depletion of my-HSCs selectively increased both naïve T cells and mature B cells in aged mice.

My-HSC depletion lowers aging phenotypes

In addition to their decreased frequency and production in aged animals, lymphocytes undergo age-related accumulation of markers of exhaustion and/or inflammation thought to contribute to immune decline[41]. In aged mice, CD4 T cells with an ‘exhausted’ phenotype ($PD1^{+}CD62L^{-}$) increase relative to those with a ‘non-exhausted’ phenotype ($PD1^{-}CD62L^{+}$)[41], which we confirmed in our experimental cohort (Fig. 3g). Compared to aged controls, antibody-conditioning decreased CD4+ $PD1^{+}CD62L^{-}$ cells relative to CD4+ $PD1^{-}CD62L^{+}$ cells (Fig. 3g). Aged mice also accumulate ‘age-associated B cells’ (ABCs) correlated with reduced humoral immunity[42]. Our control cohort of aged mice had an increased frequency of ABCs ($CD19^{+}IgM^{+}CD93^{-}CD43^{-}$ $CD21/CD35^{-}CD23^{-}$)[42] relative to young-adult mice, which was significantly decreased after antibody-conditioning (Fig. 3h). Thus, in addition to increasing naïve T cells and mature B cells, antibody-conditioning also suppressed lymphocyte age-related immunophenotypes. Collectively, these results suggested my-HSC depletion might enhance immune function in aged animals.

My-HSC depletion lowers systemic markers

In addition to immune cell phenotypes, aging is associated with increased levels of circulating pro-inflammatory mediators, referred to as ‘inflammaging’, which has been linked to HSC dysfunction and myeloid-bias[14]. To determine if my-HSC depletion in aged animals impacted pro-inflammatory mediators, we evaluated circulating proteins in plasma from young-adult and aged mice, with or without antibody-conditioning, after approximately 8-weeks. The most elevated proteins in aged mice relative to young-adult mice were the pro-inflammatory factors IL-1α[43] and CXCL5[14] (Extended Data Fig. 6b), which were also the most decreased proteins in aged mice receiving antibody-conditioning (Fig. 3i-j, Extended Data Fig. 6c-d). Antibody-conditioning decreased additional pro-inflammatory mediators in aged mice, including IL-1β[44], CXCL2 (MIP-2) [14,44], and IL-23 (Fig. 3j, Extended Data Fig. 6c, 6e). Thus, in addition to resulting in a more youthful composition of immune cells, my-HSC depletion decreased the levels of circulating pro-inflammatory mediators several months after treatment.

My-HSC depletion enhances aged immunity

A hallmark of immune aging is reduced resistance to infection and responsiveness to vaccination[13], as became evident during the COVID-19 pandemic[45]. To determine if my-HSC depletion enhanced functional immunity to infection, we examined the immune responses of mice to live-attenuated virus and subsequent challenge with a pathogenic viral infection using the murine Friend retrovirus (FV) model[46,47]. Immune protection against FV involves a complex immune response that requires B cells and CD4+ and CD8+ T cells, each providing indispensable and non-redundant functions[48-51]. The stringent immunological requirements for vaccine protection in the FV model provided a rigorous test for rejuvenation of immune responses in aged mice.

The generation of antigen specific antiviral CD8+ T cells is required for live-attenuated vaccine-induced immune protection from FV. To evaluate the primary response to vaccination, aged mice were vaccinated intravenously with live-attenuated virus approximately 8-weeks after receiving anti-NEO1 containing antibody-conditioning. The spleens were harvested for analysis 10-14 days later at the peak of CD8+ T cell response. Aged mice receiving my-HSC depletion demonstrated increased virus-specific CD8+ T cell responses (dextramer+) in the spleen following vaccination compared to aged controls (Fig. 4b), demonstrating that my-HSC depletion improved the primary response to live-attenuated viral infection. To evaluate immune protection, aged mice were vaccinated approximately 8-weeks after receiving anti-NEO1 antibody-conditioning and then challenged with pathogenic FV 6-weeks after vaccination (Extended Data Fig. 9a). Spleen cells were examined at two-weeks post-infection, the peak of FV replication. We verified that anti-NEO1 antibody conditioning decreased my-HSC by both frequency and absolute number under these conditions and time-points (Fig. 4a, Extended Data Fig. 9c-h). Control young-adult mice inoculated with FV had approximately three-fold larger spleens than naïve controls (Fig. 4c) and a per-spleen median of 7,000 infectious centers (Fig. 4d), a measure of live, infectious virus. Vaccination of young-adult mice prevented splenomegaly (Fig. 4c) and significantly reduced infectious centers (Fig. 4d). Aged-infected mice fared much worse than young-adult mice. Their median increase in spleen weights was ten-fold (Fig. 4c) and their median infectious centers per spleen was 4 million (Fig. 4d), more than 500-fold the median in infected young-adult mice. Vaccination of aged mice resulted in a slight but not statistically significant decrease in splenomegaly (Fig. 4c), and only 1 out of 8 mice was able to control infection (Fig. 4d, Extended Data Fig. 9j). In contrast, mice that had been conditioned by my-HSC depletion 2-months prior to vaccination demonstrated significantly reduced splenomegaly (Fig. 4c), and 4 of the 9 my-HSC-depleted mice had no detectable infectious centers in their spleens (Fig. 4d), the most stringent test of infection control. Compared to age-matched controls, vaccinated and infected aged mice receiving my-HSC depletion had increased virus-specific CD8+ T cell responses (dextramer+) in the spleen (Fig. 4e), which was correlated with protection (Extended Fig. Data 9k). Taken together, these results demonstrated that my-HSC depletion in aged mice significantly improved immune responses to live viral infections.

My-HSC genes are expressed by human HSCs

The age-associated expansion of HSCs with myeloid bias occurs in both mouse and humans[3]. Having demonstrated that antibody-mediated depletion of my-HSC reverses several features of age-related immune decline in mice, we investigated if the my-HSC antigenic targets used in our conditioning protocol might be applicable to humans. First, we sought to determine if human homologs to mouse my-HSC genes were expressed by aged human HSCs. Indeed, several mouse my-HSC genes, including CD62p (*Selp*), CD150 (*Slamf1*) [52], and CD41 (*Itga2b*), were significantly increased in aged human HSCs from independent datasets[3,53-55] (Fig. 5a-b, Extended Data Fig. 10a-b) and were correlated with age across adulthood (Fig. 5c-e, Extended Data Fig. 10c-e). In addition, genes for multiple mouse my-HSC antigens were enriched in HSCs isolated from pathologies related to aging of the human hematopoietic system, including aberrant[56,57] and pre-malignant human HSCs[58] (Extended Data Fig. 10f). Interestingly, the most enriched gene across all datasets – in both mouse and human – was CD62p. Thus, several genes for mouse my-HSC antigens were also enriched in human HSCs associated with age and disease.

We next evaluated if any candidate markers could be detected on human HSCs with antibodies. We examined the cell-surface protein expression of a subset of candidate antigens on highly pure populations of human HSCs ($Lin^-CD34^+CD38^-CD90^+CD45RA^-$)[67], which represent <10% of $CD34^+$ cells in bone marrow (Extended Data Fig. 10g-h). We previously demonstrated that antibodies to NEO1 marked a subpopulation of human HSCs[19]. Antibodies to several cell-surface candidates – including CD62p and CD150 – also separated human HSCs into two populations (Fig. 5f-i, Extended Data Fig. 10j-m). These markers were expressed with varying degrees of enrichment on HSCs relative to downstream progenitors (Extended Data Fig. 10n-s). Thus, all three mouse my-HSC markers that we demonstrated as therapeutic targets for my-HSC depletion *in vivo* – CD150, CD62p, and NEO1 – were also present on the cell-surface of a subset of human HSCs. These experiments represent the first steps towards identifying therapeutic targets to deplete human my-HSCs and to rejuvenate the aged immune system with this strategy (Extended Data Fig. 10t).

Discussion

Evolution of the vertebrate immune system occurred in geographically limited populations. Before machine-mediated transportation – trains, planes, boats and cars – individuals were likely to be exposed to the majority of pathogens in their local geography by the time of reproductive age. Since T and B memory/stem cells can survive an individual's lifetime[68,69], they should be sufficient to provide adaptive immune memory to all local pathogens. Thus, the generation of new T and B lymphocytes in later life was likely no longer advantageous, while the production of short-lived myeloid cells would remain important for acute innate responses, even in later life.

The requirement to maintain myeloid output for acute responses in the context of a long-lived memory T and B cell repertoire could explain the shifting of the HSC pool from bal-HSCs to my-HSCs during aging. Although this biology has worked well throughout almost

all of human evolution, the introduction of geographic migration by modern transportation created novel exposures of individuals to pathogens first encountered later in life when T and B cells are no longer efficiently produced. The hematopoietic system shift to myeloid-biased production has likely enabled novel pathogens to cause global pandemics. As the COVID-19 pandemic demonstrated, elderly patients are the most likely to die from SARS-CoV-2 infection[70]. In addition to poor adaptive immunity, the morbidity of elder patients infected with new respiratory pathogens such as SARS-CoV-2 is also likely due to aberrant inflammatory responses[59,71]. Thus, since my-HSCs give rise to pro-inflammatory myeloid cells, we propose that their expansion in the elderly is a double-edged sword in the battle with novel pathogens, resulting not only in a poor adaptive immune response, but also in detrimental inflammatory responses. Rejuvenating the immune system by my-HSC depletion could promote more functional immune responses by increasing the generation of new T and B cells and also by reducing the production of inflammatory myeloid cells.

Our results indicate that my-HSC depletion in aged mice enabled bal-HSCs to rebalance the hematopoietic system and restore youthful immune features, including increased lymphocyte progenitors and naïve cells, decreased markers of lymphocyte dysfunction/exhaustion, and decreased inflammatory mediators. Importantly, HSC rebalancing also improved protective immunity in aged mice to live, pathogenic retroviral infection. The murine my-HSC antigens mark subsets human HSCs, implicating them as candidate targets for human rejuvenation. Further research will be required to optimize conditioning protocols, possibly using combinations of antibodies against my-HSC-specific markers while considering possible effects on differentiated cells such as regulatory T cells[60].

Aged humans not only have polyclonal contributions of HSCs to the blood system, but many individuals also display increases of HSC clones driven by loss of function of epigenetic modifiers (e.g., TET2[61] and DNMT3A[62]) [63]. While such clones exist in many otherwise normal individuals, as observed in clonal hematopoiesis of indeterminate potential (CHIP)[64], they have a higher likelihood of progressing to MPN, MDS, and AML[69], and of developing atherosclerosis[65,66]. It is conceivable that amongst my-HSCs are those that are involved in CHIP and could progress to these myeloid diseases, AML, and the inflammations that occur in other age-related inflammatory and fibrotic conditions[66]. Rejuvenating the immune system with bal-HSCs could also restore the surveillance systems required for elimination of transformed and partially transformed cells that drive cancer, and/or reduce the generation of myeloid cells that suppress tumor immunity. Such an approach could support both T-cell based and myeloid-based immunotherapies, or reverse the inflammation and/or depletion of cells that result from cytotoxic anti-cancer therapies including chemotherapy and radiotherapy. Our study provides proof-of-principle for translational studies focused on applying similar strategies to improve functional immunity combat infections, chronic disease, and cancer.

The conservation between mouse and humans of the expansion of myeloid-biased HSCs and of the genes that increase during HSC aging suggests that this pre-clinical study could support the development of clinical therapies to rejuvenate the blood-forming system in patients. These mouse studies herein point the direction of which markers on human my-HSC may be effective or reasonable targets. Further pre-clinical and clinical studies

will be required to determine if such a therapy will be feasible in humans. The clinical development of safe protocols to rebalance HSCs could have broad impacts on a number of age-associated issues.

Methods

Animal Experiments

All mice were C57BL/6 or (C57BL/10 × A.BY)F1 (H-$2^{b/b}$, $Fv1^{b}$, $Rfv3^{r/s}$) and between 8-weeks to 120-weeks old. For transplant experiments, C57BL/6J (Jackson Labs, Strain #000664) CD45.2 mice were donors and B6.SJL-$Ptprc^{a}$ $Pepc^{b}$/BoyJ (Jackson Labs, Strain #002014) CD45.1 mice were recipients. Mouse ages are described in the figure legends. Mice were routinely monitored, and sick or diseased mice were excluded from further analysis. Mice were housed in individually ventilated cages, same-sex, on a 12-hour light cycle, with temperature and humidity control, enrichment material, and ab libitum rodent chow and water. Mice were bred and maintained at Stanford University's Research Animal Facility or at the Rocky Mountain Laboratories. All animal experiments were performed according to guidelines established by the Administrative Panel on Laboratory Animal Care of Stanford University or on an Animal Study Proposal approved by the Animal Care and Use Committee of the Rocky Mountain Laboratories (RML 2018-058, RML 2021-046) and carried out by certified staff in an Association for Assessment and Accreditation of Laboratory Animal Care International-accredited facility according to the institution's guidelines for animal use, the basic principles in the NIH Guide for the Care and Use of Laboratory Animals, the Animal Welfare Act, and the United States Department of Agriculture and the United States Public Health Service Policy on Humane Care and Use of Laboratory Animals.

Bone Marrow Cell Isolation

Mice were euthanized and bone marrow was harvested following one of two methods. The unilateral or bilateral femurs, tibias, and pelvises were dissected, cleaned, and collected in a mortar bowl containing PBS supplemented with 2% FBS (FACS-buffer) and DNAse-I (LS002007; Worthington). Bones were crushed, and the resulting cell suspension was passed through a 40μm filter. Alternatively, the femurs and tibias were dissected, cleaned, and cut at the joints and the bone marrow was flushed using an inserted 25-gauge needle and phosphate-buffered balanced salt solution (PBBS) with cells passed through a 100μm filter. Cells were collected by centrifugation and washed with FACS-buffer multiple times. Red blood cells were depleted by ACK-lysis or by cKIT-enrichment. For ACK-lysis, cells were resuspended in 1mL ACK Lysing Buffer (A1049201; ThermoFisher) and incubated for 10 minutes at room-temperature. For cKIT-enrichment, cells were Fc-blocked by incubation with 1mg/mL rat IgG (ab37361; abcam) for 30 minutes on ice, followed by the addition of anti-cKIT APC-eFluor780 (47-1171-82; ThermoFisher) for 30 minutes. Cells were collected by centrifugation and resuspended in FACS-buffer containing 10uL antiAPC MicroBeads (130-090-855; Miltenyi Biotec) and incubated for 20 minutes on ice. Cells were then washed and isolated with LS Columns (130-042-401; Miltenyi Biotec) using a MACS Separator (Miltenyi Biotec) according to manufacturer instructions.

Flow cytometry

Flow cytometry was performed on a FACS Aria II (BD Biosciences) or FACS Symphony (BD Biosciences) and data was collected using FACSDiva Software (BD). For absolute cell counts, cells were counted prior to flow-cytometry, or a known volume of Precision Count Beads™ (424902; BioLegend) was added to a known volume of cells, and calculations were performed according to manufacturer's instructions. For all experiments with Precision Count Beads™, the stock concentration was assumed to be $1x10^6$ particles/mL, per manufacturer. For mouse flow-cytometry, analysis was performed on whole-bone marrow or on cKIT-enriched cells, isolated as described above. Prior to antibody staining, cells were Fc-blocked by incubation with 1mg/mL rat IgG (ab37361; abcam) for 30 minutes on ice. Antibody staining was performed in FACS-buffer solution (PBS with 2% FBS and DNAse-I). Incubations were performed on ice for at least 30 min. For HSC and progenitor analysis[72-75], cells were stained with combinations of the following antibodies (hereafter: HSPC stain): anti-FLT3 APC 1:50 (ThermoFisher; 17-1351-82) or anti-FLT3 PerCP-eFluor710 1:50 (eBioscience; 46-1351-82), goat anti-mouse NEO1 15ug/mL (R&D; AF1079), anti-CD150 PE-Cy7 1:50 (BioLegend; 115914; clone TC15-12F12.2), anti-IL7Ra PE-Cy5 1:25 (ThermoFisher; 15-1271-82 or BioLegend; 135016) or anti-IL7Ra APC 1:25 (BioLegend; 135012), anti-CD16/32 BV510 1:50 (BioLegend; 101308), anti-cKit APC-eFluor780 1:50 (ThermoFischer; 47-1171-82), anti-mouse Lineage Cocktail (includes anti-CD3, anti-Ly-6G/C, anti-CD11b, anti-CD45R, anti-Ter-119) AF700 1:10 (BioLegend; 133313), anti-CD48 BV711 1:50 (BD; 740687), anti-CD41 BV650 1:50 (BD; 740504), anti-CD34 biotin 1:50 (ThermoFisher; 13-0341-85), anti-SCA1 BUV395 1:50 (BD; 744328), followed by Streptavidin BUV737 1:50 (BD; 612775) and donkey anti-goat IgG H&L AF488 1:100 (abcam; ab150129). In some instances, anti-CD150 clone mShad150 PE 1:50 (eBioscience; 12-1502-80) or PE-Cy7 (eBioscience; 25-1502-82), anti-CD150 clone 9D1 PE 1:50 (eBioscience; 12-1501-80), anti-CD150 clone Q38-480 PE 1:50 (BD; 562651), anti-CD62p PE 1:50 (BioLegend; 148308), or anti-Ly6D PE 1:50 (eBioscience; 12-5974-80), were included. For testing of candidate my-HSC markers, the following antibodies were used: anti-CD51 PE 1:50 (12-0512-81; ThermoFisher), anti-CD61 PE 1:50 (561910; BD), anti-CD31 PE 1:50 (561073; BD), anti-CD38 PE 1:50 (12-0381-81; ThermoFisher), anti-CD47 clone MIAP301 PE 1:50 (127507; BioLegend), anti-CD47 clone MIAP410 PE 1:50 (LS-C810701-25; LSBio), anti-CD62p PE 1:50 (148305; BioLegend), anti-ALCAM PE 1:50 (12-1661-82; ThermoFisher), anti-CD9 PE 1:50 (124805; BioLegend), anti-ESAM PE 1:50 (136203, BioLegend), anti-TIE2 PE 1:50 (124007; BioLegend), anti-CD201 PE 1:50 (141503; BioLegend), or anti-cKIT clone ACK2 PE 1:50 (135105; BioLegend). The my-HSC fold-enrichment for each marker was calculated as: (% marker positive of my-HSC)/(% marker positive of bal-HSC). To calculate the absolute number of HPCs (e.g., CMP&GMP, MkP, MEP, CLP, etc.) the absolute numbers of cells was quantified in total bone marrow (non-cKIT enriched). To quantify the absolute number of HSCs and HSC subsets (e.g., my-HSCs, bal-HSCs, etc.), the absolute numbers of cells was quantified in total bone marrow (non-cKIT enriched), or the percentage of HSC/HSC subsets per KLS (Lin^- $cKIT^+Sca1^+$) cells was calculated in the cKIT-enriched fraction and multiplied by the total number of KLS cells quantified in a paired sample of total bone marrow (non-cKIT enriched).

For T cell analysis, cells were stained with the following antibodies: anti-Helios AF647 1:200 (BD; 563951), anti-CD3 APC-Cy7 1:200 (BioLegend; 100222), anti-Ki67 R718 1:150 (BD; 566963), anti-CD43 AF488 1:400 (BioLegend; 121210), anti-CD8 BUV395 1:400 (BD; 563786), anti-Foxp3 eF450 1:150 (Invitrogen; 48-5773-82), anti-CD4 BV510 1:400 (BioLegend; 100559), anti-CD44 BV605 1:400 (BD; 563058), anti-CD62L BV711 1:1,000 (BioLegend; 104445), anti-EOMES PE 1:200 (Invitrogen; 124875-82), anti-PD1 PE-CF594 1:200 (BD; 562523), anti-Tbet PE-Cy7 1:200 (Invitrogen; 25-5825-82), anti-CD25 PerCP-Cy5.5 1:200 (BioLegend; 102030). FV-specific $CD8^+$ T cells were identified using H-$2D^b$/Abu-Abu-L-Abu-LTVFL APC-or PE-D^bgagL-MHC Dextramer (Immudex, Copenhagen, Denmark) at 1:25 during surface staining. For B cells analysis, cells were stained with the following antibodies: anti-CD43 APC 1:400 (BioLegend; 121214), anti-CD21/CD35 APC-Cy7 1:400 (BioLegend; 123418), anti-CD5 AF700 1:200 (BioLegend; 100636), anti-IgM FITC 1:400 (Invitrogen; 11-5790-81), anti-CD19 BUV395 1:400 (BD; 563557), anti-IgD eFluor450 1:400 (eBioscience; 48-5993-82), anti-CD11b BV510 1:400 (BioLegend; 101245), anti-MHCII BV605 1:400 (BD; 563413), anti-CD40 BV711 1:400 (BD; 740700), anti-PDL1 PE 1:200 (Invitrogen; 12-5982-82), anti-CD93 PE-Cy7 1:400 (BioLegend; 136506), anti-CD23 PerCP-Cy5.5 1:200 (BioLegend; 101618), and anti-CD45R/B220 PE-CF594 1:800 (BD; 562290). Intracellular staining was performed as described[76].

For peripheral blood chimerism analysis, cells were stained with the following antibodies: anti-CD8a Spark UV387 1:50 (BioLegend; 100797), anti-CD4 BUV737 1:200 (BD, 612843), anti-Gr1 Pacific Blue 1:100 (BioLegend, 108429), anti-CD3 BV711 1:100 (BioLegend, 100241), anti-CD44 BV785 1:300 (BioLegend, 103059), anti-CD45.2 AF488 1:100 (BioLegend, 109815), anti-Foxp3 PE 1:100 (eBioscience, 12-5773-82), anti-CD62L PE/Dazzle™ 594 1:200 (BioLegend, 104447), anti-CD19 PE-Cy7 1:100 (BioLegend, 115519), anti-CD45.1 APC 1:50 (BioLegend 110713), anti-CD11b APC-Cy7 1:100 (BioLegend, 101225). Intracellular staining was performed with Foxp3 Transcription Factor Staining Buffer Set (eBioscience, 00-5523-00) per manufacturer's protocol. Red blood cells were removed with ACK lysis buffer (Gibco, a1049201). Non-specific binding was prevented with TruStain FcX PLUS (BioLegend cat# 156604). To determine viability of fixed cells, cells were incubated in buffer containing LIVE/DEAD™ Fixable Aqua Dead Cell (ThermoFisher; L34957).

For erythroid cell analysis, spleen cells were first incubated for 30 min with mAb 34, a mouse IgG2b specific for the FV glycoGag protein expressed on infected cells[77], then stained with anti-mouse IgG2b FITC (BD; 553395) and anti-Ter119 PE-Cy7 (Invitrogen; 25-5921-82). Cells from uninfected controls were used for gating strategy. For non-fixed cells, to determine viability, cells were incubated in buffer containing SYTOX Red Dead Cell Stain (Life Technologies) or SYTOX Blue Dead Cell Stain (ThermoFisher; S34857).

For flow-cytometry computational analysis[78,79], samples were first analyzed in FlowJo v10 Software (BD Life Sciences) and the T cell (CD4+ and CD8+) gated events were down-sampled to an equivalent number of cells per condition (Young, Aged, Aged+Conditioning), and the channel data for each sample was exported as CSV files. The Spectre package[80] was applied to data from all samples using R (version 4.2.2), which were annotated and merged,

and clusters were assigned with PhenoGraph[81], followed by dimensionality reduction with Uniform Manifold Approximation and Projection (UMAP) [82] for visualization. Cluster assignments were annotated and/or merged based on prior knowledge of phenotypes for naïve, central memory (CM), and effector memory (EM) T cell subtypes.

To identify anti-CD150 antibodies that are not blocked by anti-CD150 antibody clone 1 (TC15-12F12.2, TC15), bone-marrow HSPC stained cells were incubated with saturating concentrations (200ug/mL) of unlabeled anti-CD150 antibody clone TC15 and then stained with PE-conjugated anti-CD150 clones 2 (Q38), 3 (9D1), or 4 (mShad150); PE-Cy7 conjugated anti-CD150 clone TC15 was used as a control. To confirm if any anti-CD150 clones identify the same population of cells as anti-CD150 antibody clone 1 (TC15) by flow-cytometry, bone-marrow HSPC stained cells were incubated with PECy-7 anti-CD150 antibody clone 1 (TC15) and with either PE-conjugated anti-CD150 clone 2 (Q38), 3 (9D1), or 4 (mShad150). To confirm that anti-CD150 antibody clone 4 (mShad150) does not block anti-CD150 clone 2 (Q38), bone-marrow cells were incubated with saturating concentrations (200ug/mL) of unlabeled anti-CD150 clone mShad150 and then stained with PE-conjugated anti-CD150 clone Q38; PE-Cy7 conjugated anti-CD150 clone mShad150 was used as a control. To confirm that anti-CD150 clone mShad150 and clone Q38 identify the same populations by flow-cytometry, bone-marrow cells were incubated with PECy-7 anti-CD150 clone mShad150 and with PE anti-CD150 clone 2 (Q38).

To confirm that mouse IgG2a (SB115d; SouthernBiotech) and IgG2b (SB115h; SouthernBiotech) anti-goat antibodies do not block donkey anti-goat IgG AF488 (abcam; ab150129), bone-marrow HSPC stained cells were incubated with saturating concentrations (100ug/mL) of unlabeled mouse IgG2a (615801; SouthernBiotech) or IgG2b (6157-01; SouthernBiotech) anti-goat antibodies and then stained with donkey anti-goat AF488. To confirm that mouse IgG2a and IgG2b anti-goat antibodies identify the same populations as donkey anti-goat IgG AF488 by flow-cytometry, bone-marrow HSPC stained cells were incubated with mouse IgG2a AF555 1:100 (6158-32; SouthernBiotech) or IgG2b PE 1:100 (6157-09; SouthernBiotech) anti-goat antibodies, and with donkey anti-goat AF488.

For human HSC[83] flow-cytometry analysis, bone marrow mononuclear cells from young-adult donors (ages 26-33) were commercially obtained (AllCells, Inc.). CD34-positive cells were enriched with CD34 MicroBead Kit (130-046-702; Miltenyi Biotec) according to manufacturer instructions. Antibody staining was performed in FACS-buffer solution (PBS with 2% FBS and DNAse-I) at a 1:1 ratio to Brilliant Stain Buffer (563794; BD Biosciences). Non-specific binding was blocked with FcR Blocking Reagent (130059-901; Miltenyi Biotec) for 5 minutes on ice, followed by the addition of the following antibodies: antilineage panel PE-Cy5: [anti-CD3 1:200 (BD; 555341), anti-CD4 1:200 (BD; 555348), anti-CD8 1:200 (BD; 555368), anti-CD11b 1:200 (BD; 555389), anti-CD14 1:200 (ThermoFisher; MHCD1406), anti-CD19 1:200 (BD; 555414), anti-CD20 1:200 (BD; 555624), anti-CD56 1:200 (BD; 555517), anti-CD235a 1:200 (BD; 559944)], anti-CD34 APC-Cy7 1:25 (343514; Biolegend), anti-CD45RA BV-785 1:25 (304139; Biolegend), anti-CD38 APC 1:10 (555462; BD), anti-CD90 FITC 1:50 (328107; Biolegend), and one of anti-human PE: anti-CD62P clone AK4 1:20 (304905; Biolegend), anti-CD62P clone Psel.KO2.3 1:20 (12-0626-82; eBioscience), anti-CD62P clone AC1.2 1:5 (550561; BD),

anti-CD150 1:20 (306307; Biolegend), anti-TIE2 1:20 (CD202b, 334205; Biolegend), anti-ESAM 1:10 (408519; Novus), anti-CD166 1:20 (ALCAM, 343903; Biolegend), anti-CD9 1:20 (312105; Biolegend), anti-CD105 1:20 (Endoglin, 800503; Biolegend), or anti-CD304 1:20 (Neuropilin-1, 354503; Biolegend). All flow cytometry data were analyzed with FlowJo v10 Software (BD Life Sciences).

Antibody Conditioning

For antibody conditioning experiments, mice received injections of antibodies resuspended in PBS intraperitonially. Control animals received an equivalent volume of PBS or an equivalent amount of isotype control antibodies: mouse IgG1 (clone MOPC-21, Bio X Cell), rat IgG2b (clone LTF-2, Bio X Cell), or rat IgG2a (clone RTK2758, BioLegend). Given that isotype control antibodies demonstrated no impact on phenotype, PBS was used as a control in many experiments, as described[84]. My-HSC specific antibodies (anti-CD150, anti-CD62p, or anti-NEO1) were injected on Day -9. For CD150, 200μg rat IgG2b anti-CD150 (clone mShad150, eBioscience) for CD150^{v1} protocol, or 200μg rat IgG2a anti-CD150 (clone TC15-12F12.2, BioLegend) for CD150^{v2} protocol, was as administered on Day -9. For CD62p, 200μg mouse anti-CD62p (clone RMP-1, BioLegend) was administered on Day -9. For NEO1, 30μg, 90μg, or 200μg goat anti-NEO1 (polyclonal cat# AF1079, R&D) [19,85-92] was administered on Day -9 for NEO1^{v1} protocol, and when indicated, 150μg mouse IgG2a (SB115d; SouthernBiotech) or IgG2b (SB115h; SouthernBiotech) anti-goat was administered 24-hours later[93-95] on Day -8, for NEO1^{v2} protocol. For CD47-blockade, mouse IgG1 anti-CD47 (clone MIAP410, Bio X Cell) was administered on Day -11 (100μg) and on Days -9 to Day -5 (500μg daily), as previously described [34,96]. For cKIT, rat anti-cKIT (clone ACK2, Bio X Cell) was injected retro-orbitally on Day -9 (30μg, 50μg, or 100μg), and mice were administered 400μg of diphenhydramine at least 30 min prior to administration, as previously described[34,96]. Mice were euthanized for bone-marrow analysis on Day 0 (e.g., approximately 1-week), at approximately 8-10 weeks, or at approximately 14-16 weeks.

Blood Cell Isolation and Plasma Immunoassays

For blood cell isolation and plasma immunoassays, mouse peripheral blood was collected in EDTA tubes after removal of cells through centrifugation at 500 RCF for 10 min, whereupon plasma was transferred to a clean tube and centrifuged for an additional 10 min at 13,000 RCF, while the red blood cells were depleted with ACK-lysis, followed by a PBS wash, and then stained for flow cytometry as described above. For absolute cell counts per mL, the volume of blood obtained per animal was recorded, and a known volume of Precision Count Beads™ (424902; BioLegend) was added to a known volume of cells, and calculations were performed according to manufacturer's instructions assuming a Precision Count Beads™ stock concentration of 1x10^6 particles/mL. Plasma was frozen at −80C until processing by the Stanford Human Immune Monitoring Center (HIMC), as described[84]. Samples were run in technical triplicate using the 48-Plex Mouse ProcartaPlexPanel™ (EPX480-20834-901; ThermoFisher Scientific) or the Mouse Acute Phase Magnetic Bead Panel 2 (MAP2MAG-76K; Millipore Sigma). MFI average value were compared after removal of statistical outliers using the extreme studentized deviate (ESD) Grubbs statistical

test (α=0.0001) [97]. For comparison of estimated concentrations, values below the limit of detection were assigned the value equal to this lower limit.

Friend Virus Mouse Model

Ethics and biosafety statement—All in vivo experiments were performed in accordance with Animal Study Proposal approved by the Animal Care and Use Committee of the Rocky Mountain Laboratories (RML 2018-058, RML 2021-046) approved by the Institutional Animal Care and Use Committee of Rocky Mountain Laboratories (National Institutes of Health [NIH]) and carried out by certified staff in an Association for Assessment and Accreditation of Laboratory Animal Care International-accredited facility, according to the institution's guidelines for animal use, following the guidelines and basic principles in the NIH Guide for the Care and Use of Laboratory Animals[98], the Animal Welfare Act, and the United States Department of Agriculture and the United States Public Health Service Policy on Humane Care and Use of Laboratory Animals.

Vaccination and virus challenge—The Friend retrovirus (FV) stock used in these experiments was FV-NB, a lactate dehydrogenase virus (LDV)-free[99] complex containing NB-tropic Friend murine leukemia helper virus (F-MuLV) and polycythemia-inducing spleen focus-forming virus (SFFV) [100] generated as a spleen cell homogenate from infected BALB/C mice. The live attenuated vaccine was an NB-tropic F-MuLV helper stock, which replicates poorly without SFFV-induced proliferation, generated as a supernatant from infected *Mus dunni* cells[101]. *Mus dunni* cells were obtained from American Type Culture Collection (ATCC), tested negative for mycoplasma upon receipt, and were not independently authenticated beyond the provided identity. Mice of (C57BL/10 x A.BY)F1 background were vaccinated by 0.1 ml intravenous (i.v.) injection of 10^5 focus-forming units (FFU) of virus in phosphate-buffered, balanced salt solution (PBBS). For challenge, mice were injected i.v. with 0.2 ml PBBS containing 20,000 spleen focus-forming units of FV-NB complex.

Infectious centers assay—Titrations of single cell spleen suspensions were plated onto susceptible *Mus dunni* cells and allowed to incubate *in vitro* for 2 days at 37°C and 5% CO2. The plates were then fixed with 95% ethanol, stained with F-MuLV envelope-specific Mab 72015[102], followed by goat anti-mouse (H+L) HRP (EMD Millipore; AP308P), and then developed with aminoethylcarbazol substrate to detect foci.

Antigen-expressing cells in vivo—To quantify Ag34+ expressing cells *in vivo*, Ag34 expression was determined by mAb 34 antibody staining by flow-cytometry[77]. Cells from uninfected controls were used to define the background level of staining. A positive vs. negative threshold was set equal to the highest level of background staining observed in non-infected animals, and only samples with values higher than this threshold were considered positive[103]. Samples with values equal to or lower than background level in non-infected animals were considered negative and their level of staining was set to a value of 0%. Both positive and negative samples were included in the statistical analysis for comparison. To obtain the absolute number of Ag34+Ter119+ cells per samples, an equivalent number of cells were analyzed for each mouse by flow-cytometry, and the frequency of Ag34+Ter119+

cells (as defined by the positive and negative thresholds) per total cells was multiplied by the total number of cells counted per spleen.

Transcriptomic Analysis

Murine and Human HSCs—The following publicly available datasets were used to compare mouse old vs. young HSCs: Beerman[16] (a, GSE43729), Bersenev[24] (b, GSE39553), Flach[25] (c, GSE48893), Maryanovich[26] (d, GSE109546), Norddahl[27] (e, GSE27686), Wahlestedt[28] (f, GSE44923), Renders[29] (g, GSE128050), Sun[30] (h, GSE47819). The following datasets were used to compare mouse myeloid-biased HSCs vs. balanced HSCs: Gulati[19] (i, GSE130504), Montecino-Rodriguez[22] (j, GSE112769) Sanjuan-Pla[21] (k, E-MEXP-3935). The following publicly available datasets were used to compare human old vs. young HSCs: Pang[3] (a, GSE32719), Adelman[53] (b, GSE104406), Nilsson[54] (c, GSE69408), Hennrich[55] (d, GSE115348). Additional transcriptional publicly available datasets related to human HSCs included: Kumar[104] (e, $HMGA2^+$ vs. $HMGA2^-$ $CD34^+$ cells, GSE107594), Tong[56] (f, Essential Thrombocythemia & Polycythemia Vera vs. Normal HSCs, GSE111410), Woll[57] (g, MDS vs. Normal HSCs, GSE55689), Corces[58] (e, Pre-Leukemic vs. Normal HSCs, GSE74246). Data was processed and analyzed with GREIN[105] or GEO2R[106,107].

Murine progenitors, mature cells, and tissues—To determine gene expression of mouse progenitors and mature cells, processed data was obtained directly from Gulati Supplementary Table 1[19] on 23 hematopoietic phenotypes based on 64 microarray expression profiles extracted by the Gene Expression Commons[31]. Publicly available gene expression data from bulk mouse tissues was obtained from: *Tabula Muris* (GSE132040[108]) and Kadoki (GSE87633[109]). Data was processed with Phantasus (v1.19.3) [110].

RNA-sequencing of FACS-purified mouse HSCs—For RNA-sequencing of purified mouse HSCs, approximately 1,000 total HSCs (KLS $FLT3^-CD34^-$ $CD150^+$) were FACS-sorted from aged control mice or aged mice that received antibody-conditioning 9 days earlier and immediately added to lysis buffer. Libraries were prepared using Takara SMART-Seq v4 Ultra low Input RNA kit and sequencing was performed with NovaSeq with approximately 20 million paired reads per sample by MedGenome Inc. Differential gene expression was performed using DESeq2[111] with fold change shrinkage. Heatmaps were generated using Phantasus[110] (v1.21.5) with all protein coding FPKM values filtered by minimum >0 as input and Limma[112] to define differentially expressed genes. Gene Set Enrichment Analysis (GSEA) [113] was conducted on genes ranked by DESeq2 test statistic using WEB-based GEne SeT AnaLysis Toolkit[114] (WebGestalt 2019) with default parameters using a custom list of curated gene-signatures. The following publicly available datasets were used to obtain gene-signatures Young vs. Old HSCs: Svendsen[20] (*i*), Kuribayashi[37] (*ii*), Maryanovich[26] (*iii*, GSE109546), Norddahl[27] (*iv*, GSE27686), Montecino-Rodriguez[22] (*v*, GSE112769), Wahlestedt[28] (*vi*, GSE44923), Mann (*vii*, GSE100428[18]), Renders[29] (*viii*, GSE128050). The following datasets were used to obtain gene-signatures of mouse myeloid-biased (my-) HSCs vs. balanced (bal-) HSCs: Mann[18] (*i*, GSE100428), Montecino-Rodriguez[22] (*ii*, GSE112769), Gulati[19] (*iii*, GSE130504). Gene-signatures were obtained directly from these studies or were generated by identifying

statistically significant differentially expressed genes between cell populations. Data was processed and analyzed with GREIN[105] or GEO2R[106,107].

HSC transplant experiments

For HSC transplant experiments, 100 total HSCs (KLS FLT3$^-$CD34$^-$CD150$^+$) were FACS-sorted from CD45.2 aged control mice, or CD45.2 aged mice that received antibody-conditioning 9 days earlier, and were injected retro-orbitally into 2-month-old recipient CD45.1 mice together with 1x10^6 whole-bone marrow CD45.1 support cells in 100uL PBS. Recipient mice received split-dose irradiation 24 hours prior to transplantation with 2 doses of 4.5Gy 4 hours apart. For chimerism analysis, peripheral blood was collected from the facial vein. HSC-derived donor cells were identified based on CD45.2 expression and host recipient cells were identified based on CD45.1 expression. All transplanted mice with chimerism above 0.05% were analyzed. Myeloid cells were defined as CD11b$^+$CD3$^-$CD19$^-$ and lymphoid cells were defined as CD19$^+$ or CD3$^+$. The CD45.2 HSC donor-derived Myeloid-to-Lymphoid cell ratio was calculated as: (# of CD45.2 myeloid cells) / (# of CD45.2 lymphoid cells). The Myeloid-to-Lymphoid percentage of donor cell chimerism ratio was calculated as: (% of all myeloid cells that are CD45.2) / (% of all lymphoid cells that are CD45.2).

Statistics and Reproducibility

All exact *P* values are provided in the Source Data. For all experiments, *n* indicates biologically independent replicates. The sample size for *in vivo* experiments, including antibody-depletion, viral infection, and transplantation was selected based on prior publications with similar experiments[5,19,34,35,48,49,51,96]. For all experiments, allocation of mice into experimental groups was randomized after matching for age and sex. Investigators were not blinded during data collection or analysis. All experiments involved internal control groups. Experimental and control animals were treated equally. All attempts at replication were successful. Replicated experiments were identically or similarly designed. Some experiments were replicated at independent institutions and with independent mouse strains. Data depicts combined results of at least 2 independent experiments (Fig. 1b-c, Fig. 1i-k, Fig. 3b, Fig. 4b-e, Fig. 5h-5i, Ex. Fig. 2g-j, Ex. Fig. 4j-q, Ex. Fig. 7a-c, Ex. Fig. 9b, Ex. Fig. 9i-k, Ex. Fig 10s), or is representative of four or more experiments (Fig. 1d-h, Ex. Fig. 2b-c), three experiments (Fig. 2c, Fig. 2f, Fig. 5f-g, Ex. Fig. 10g-j, Ex. Fig. 10o), two experiments (Fig. 3c-e, Fig. 3g, Ex. Fig. 7f-j, Ex. Fig. 8a-c, Ex. Fig. 10k-m, Ex. Fig. 10p), or one experiment (2a-b, Fig. 2d-e, Fig. 2g-k, 3f, 3h-j, 4a, Ex. Fig. 2d-f, Ex. Fig. 2k, Ex. Fig. 3a-n, Ex. Fig. 4a-i, Ex. Fig. 4r-x, Ex. Fig. 5c-s, Ex. Fig. 6a-n, Ex. Fig 7d-e, Ex. Fig. 8d-l, Ex. Fig. 9c-h, Ex. Fig. 10q-r). Biological replicates (n = individual mice) are reported in the figure legends. All statistical analysis was performed using GraphPad Prism (GraphPad Software) or SPSS Statistics (IBM), unless otherwise specified. The statistical tests used (parametric or non-parametric t-test, one-way ANOVA, Pearson or Spearman correlation) and details (sample size, one-or two-tailed, multiple comparison adjustment) are noted in the figure legends. Error bars denote mean +/− s.e.m., unless otherwise specified. For *p*-values, **P*<0.05, ** *P* <0.005, *** *P*<0.0005.

Extended Data

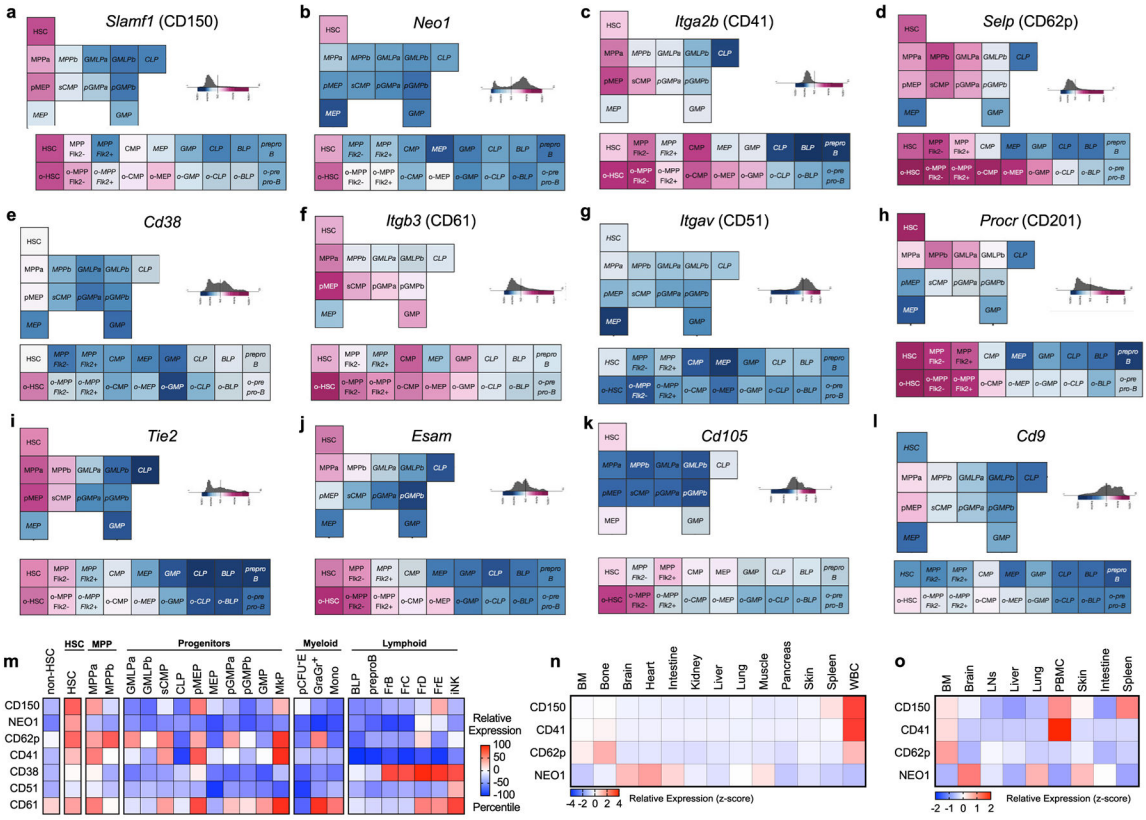

Extended Data Figure 1 | Expression of my-HSC markers in HSPCs, mature cells, and tissues

a-l, Expression of my-HSC candidate markers, *Slamf1* (CD150) (**a**), *Neo1* (NEO1) (**b**), *Itga2b* (CD41) (**c**), *Selp* (CD62p) (**d**), *Cd38* (CD38) (**e**), *Itgb3* (CD61) (**f**), *Itgav* (CD51) (**g**), *Procr* (CD201) (**h**), *Tie2* (**i**), *Esam* (**j**), *Eng* (CD105) (**k**), *Cd9* (CD9) (**l**), in HSC and HSPCs in normal mouse BM (top panels), and in young versus old bone marrow (bottom panels). Data from **a–l** obtained directly from Gene Expression Commons[31]; scale bars represent log2 Signal Intensity (*top*) and Gene Expression Activity (*bottom*) as defined by Gene Expression Commons[31]. **m**, Heatmap of relative RNA expression for CD150 (*Slamf1*), NEO1 (*Neo1*), CD62p (*Selp*), CD41 (*Itga2b*), CD38 (*Cd38*), CD51 (*Itgav*), and CD61 (*Itgb3*) in HSCs, MPPs, Progenitors, Myeloid, and Lymphoid cells. Processed data for 23 cell types were obtained directly from Gulati[19] Supplementary Table 1. Fold-enrichment = [(average percentile of HSCs)/(average percentile of all other cell types)+100], as described in this publication. **n–o**, RNA expression of CD150 (*Slamf1*), NEO1 (*Neo1*), CD62p (*Selp*), and CD41 (*Itga2b*) in bulk mouse tissues from two independent datasets: *Tabula Muris*[108] (**n**) or Kadoki[109] (**o**). For **n–o**, Values are z-score normalized for each gene across all tissues.

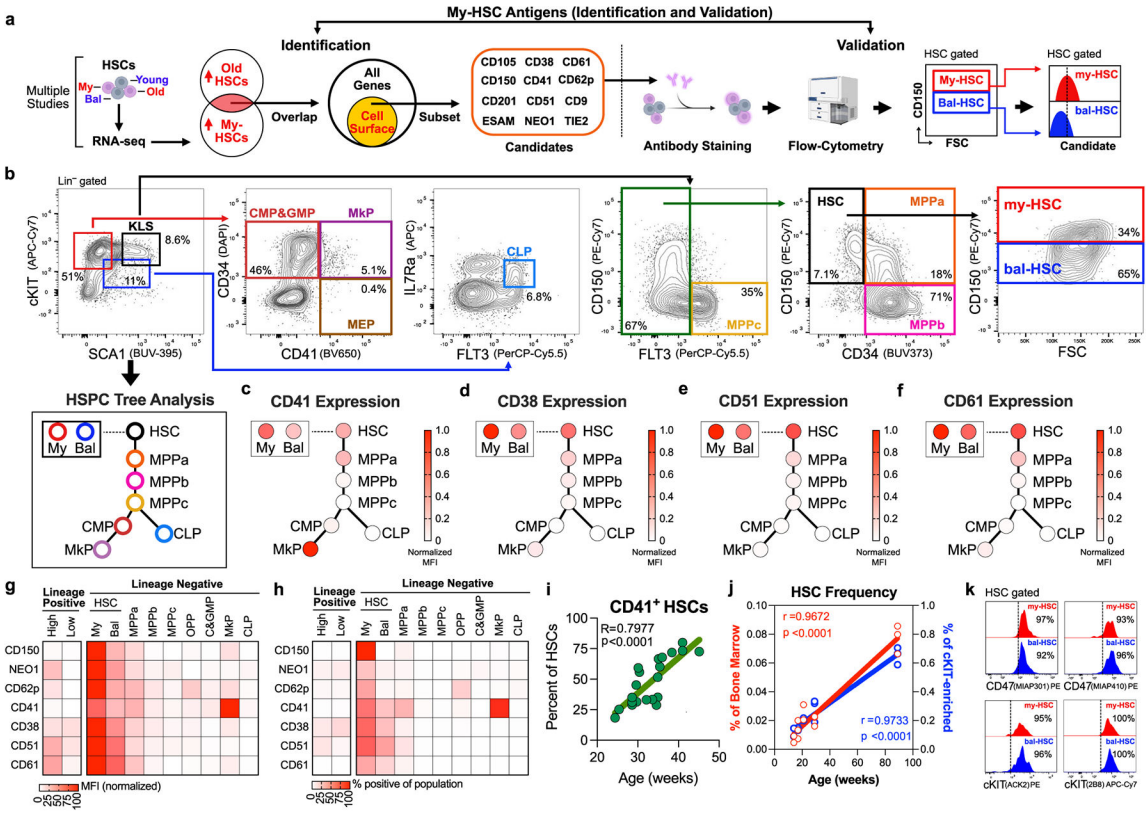

Extended Data Figure 2 | Gating strategy for total HSCs, my-HSCs, bal-HSCs, and HPCs

a, Schematic to identify and validate my-HSC cell-surface antigens. **b**, Representative flow-cytometry gating of mouse BM to identify total HSC ($Lin^-cKIT^+Sca1^+FLT3^-CD34^-CD150^+$), my-HSC ($Lin^-cKIT^+Sca1^+FLT3^-CD34^-CD150^{High}$), bal-HSC ($Lin^-cKIT^+Sca1^+FLT3^-CD34^-CD150^{Low}$), MPPs[115] [MPPa ($Lin^-cKIT^+Sca1^+FLT3^-CD34^+CD150^+$), MPPb ($Lin^-cKIT^+Sca1^+FLT3^-CD34^+CD150^-$), MPPc ($Lin^-cKIT^+Sca1^+FLT3^+CD34^+CD150^-$)], OPP ($Lin^-cKIT^+Sca1^-$), CMP&GMP ($Lin^-cKIT^+Sca1^-CD34^+CD41^-$), MkP ($Lin^-cKIT^+Sca1^-CD34^+CD41^+$), MEP ($Lin^-cKIT^+Sca1^-CD34^-CD41^+$), CLP ($Lin^-cKIT^{Lo}Sca1^{Lo}IL7Ra^+FLT3^+$). Panels are after excluding dead cells, doublets, and lineage-positive ($CD3^+$, or $Ly\text{-}6G^+/C^+$, or $CD11b^+$, or $CD45R^+$, or $Ter\text{-}119^+$) cells. Used for Fig. 1b-k, Fig. 2a-f, Fig. 3b-d, Fig. 4a, Ex. Data Fig. 2c-k, Ex. Data Fig. 3a-l, Ex. Data Fig. 4a-s, Ex. Data Fig. 5c-s, Ex. Data Fig. 6a Ex. Data Fig. 8c-h. Illustration of Hematopoietic Stem and Progenitor Cell (HSPC) Tree Analysis. CMP is combined CMP&GMP. Gate to define my-HSC vs. bal-HSC was set as described previously[5]. **c–f**, Relative expression of CD41 (**c**), CD38 (**d**), CD51 (**e**), CD61 (**f**), on HSC and HSPCs. MFI values for each marker were obtained for each population and normalized from 0–1 based on the lowest to highest expression. **g–h**, Relative cell-surface levels (**g**) and percent-positive cells (**h**) for CD150, NEO1, CD62p, CD41, CD38, CD51, and CD61, on lineage-positive high and low cells, total HSCs, and HPCs in the BM. For cell-surface levels (**g**), MFI values for each marker were obtained for each population and normalized from 0–100 based on the lowest to highest expression. **i**, Percentage of total

HSCs that are $CD41^+$ (y-axis) vs. mouse age in weeks (x-axis); *n*=21 mice. **j**, Mouse age (x-axis) vs. the frequency of total HSCs (my-HSC+bal-HSC) as a percentage of live cells in the (i) total BM (left y-axis, *red*) or (ii) cKIT-enriched BM (right y-axis, *blue*) in untreated mice; *n*=13 mice. **k**, Percent-positive of my-HSCs vs. bal-HSCs for CD47 (**k**, top) using independent anti-CD47 clones (MIAP301, left; MIAP410, right), and for cKIT (**k**, bottom) using independent anti-cKIT clones (ACK2, left; 2B8, right). Mouse ages: 4-6 months (**b–i**, **k**), 3-23 months (**j**). For **a–k**, BM was cKIT-enriched prior to analysis. For **j**, total BM (non cKIT-enriched) was also examined. *p*-values and R values calculated with one-tailed Pearson correlation coefficient (**i–j**). *n* represents independent mice.

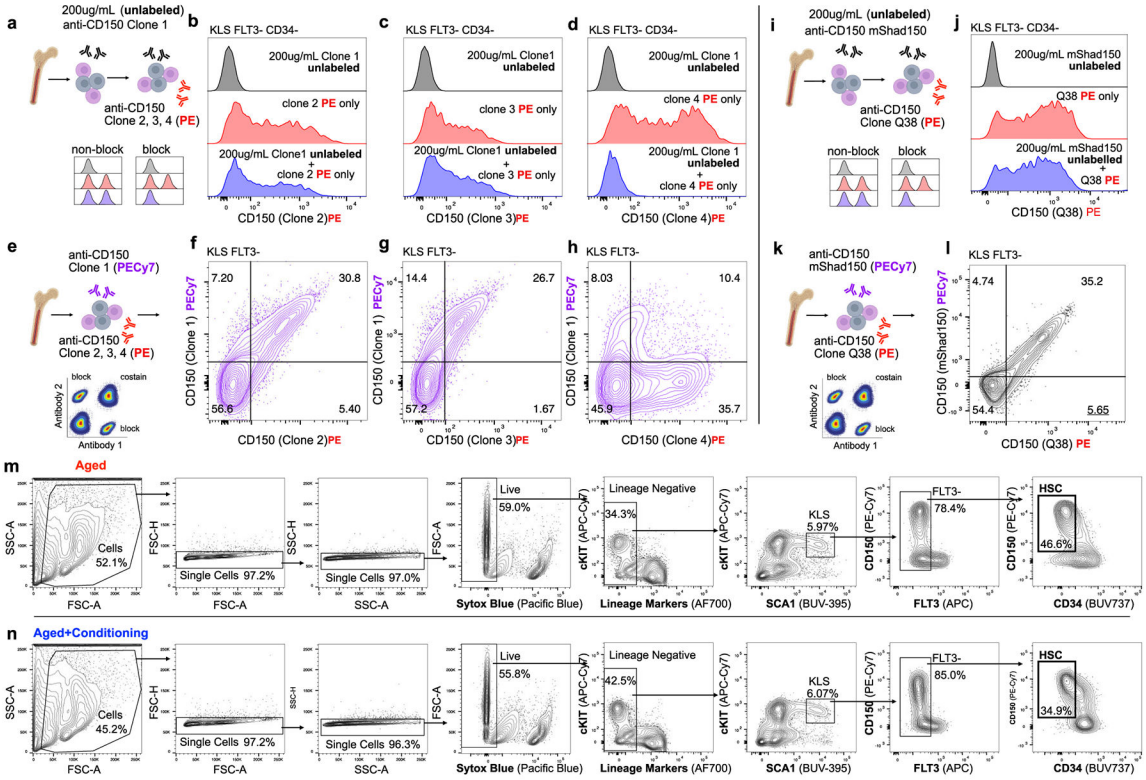

Extended Data Figure 3 | Anti-CD150 non-masking antibodies and FACS gating to isolate HSCs

a, Schematic to identify anti-CD150 antibodies not masked by anti-CD150 antibody clone 1 (TC15), used in panels **b–d**; BM cells were incubated with saturating concentrations of unlabeled anti-CD150 antibody clone 1 (TC15) and then stained with PE anti-CD150 clones 2, 3, 4 (Q38, 9D1, mShad150). **b–d**, Saturating concentrations of unlabeled anti-CD150 antibody clone TC15 blocks staining with PE anti-CD150 clone 4 (mShad150) (**d**), but does not block staining of PE anti-CD150 clones 2, 3 (Q38, 9D1) (**b–c**). **e**, Schematic to determine if anti-CD150 clones 2, 3, 4 (Q38, 9D1, mShad150) identify the same population as anti-CD150 clone 1 (TC15); used in panels **f–h**; BM cells were incubated with PECy-7 anti-CD150 antibody clone 1 (TC15) and with PE anti-CD150 clones 2, 3, 4 (Q38, 9D1, mShad150). **f–h**, Co-staining with anti-CD150 clones 2, 3 (Q38, 9D1) identifies the same population as anti-CD150 antibody clone TC15 (**f–g**). Co-staining with anti-CD150 clone 4 (mShad150) and anti-CD150 antibody clone 1 (TC15) is mutually

blocked (**h**). **i**, Schematic to identify anti-CD150 antibodies that are not blocked by anti-CD150 clone mShad150, used in panel **j**; BM cells are incubated with saturating concentrations of unlabeled anti-CD150 antibody clone mShad150 and then stained with PE anti-CD150 clone 2 (Q38). **j**, Saturating concentrations of unlabeled anti-CD150 antibody clone mShad150 does not block staining of PE anti-CD150 clone 2 (Q38) (**j**). **k**, Schematic to determine if co-staining with anti-CD150 clone 2 (Q38) identifies the same population as anti-CD150 antibody clone mShad150; used in panel **l**; BM cells are incubated with PECy-7 anti-CD150 antibody clone mShad150 and with PE anti-CD150 clone 2 (Q38). **l**, Co-staining with anti-CD150 clones 2 (Q38) identifies the same population as anti-CD150 antibody clone mShad150 (**l**). **m–n**, Representative FACS gating of mouse BM to sort total HSC ($Lin^{-}cKIT^{+}Sca1^{+}FLT3^{-}CD34^{-}CD150^{+}$) from aged (11 months) control mice (Aged, A) or aged (11 months) mice with my-HSC depletion (Aged+Conditioning, A+C), used to sort HSCs for RNA-sequencing experiment presented in Fig. 2g-h, Ex. Data Fig. 4x, and used to sort HSCs for transplant experiments presented in Fig. 2i-k, Ex. Data Fig. 4t-v. My-HSC depletion was performed with anti-NEO1+anti-CD62p+anti-cKIT+CD47 and cells were collected at day 9 post-treatment; *n*=3 mice (A), *n*=3 mice (A+C). Mouse ages approximately: 3 months (**a–h**), 5-8 months (**i–l**), 11 months (**m–n**). For (**a–n**), BM was cKIT-enriched prior to FACS analysis or sorting. *n* represents independent mice.

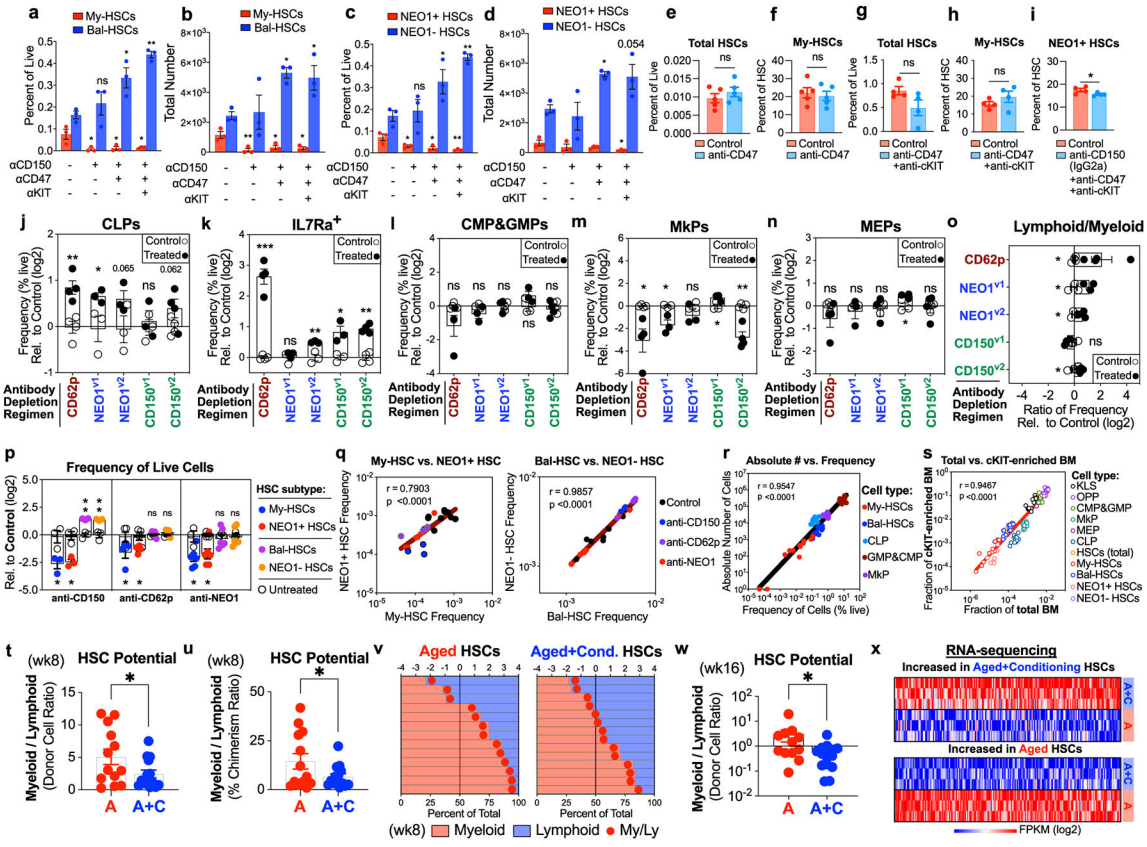

Extended Data Figure 4 l. Antibody-mediated depletion of my-HSCs *in vivo*

a–d, Frequency (% live) (**a**, **c**) or absolute number (**b**, **d**) of my-HSCs and bal-HSCs (**a–b**) or of $NEO1^{+}$ HSCs and $NEO1^{-}$ HSCs (**c–d**) after anti-CD150 conditioning (anti-CD150,

anti-CD150+anti-CD47, or anti-CD150+anti-CD47+anti-cKIT); *n*=3 mice per group. **e**, Total HSCs (my-HSCs+bal-HSCs) as percent-live in mice receiving anti-CD47; *n*=5 mice per group; *P*=0.3637. **f**, Percentage of total HSCs that are my-HSCs in mice receiving anti-CD47; *n*=5 mice per group; *P*=0.6628. **g**, Total HSCs (my-HSCs+bal-HSCs) as a percent-live, in mice receiving anti-CD47+anti-cKIT; *n*=4 mice per group; *P*=0.0973. **h**, Percentage of total HSCs that are my-HSCs in mice receiving anti-CD47+anti-cKIT; *n*=4 mice per group; *P*=0.2805. **i**, Percentage of total HSCs that are $NEO1^+$ HSCs in mice receiving anti-CD150 (IgG2a)+anti-CD47+anti-cKIT (e.g., protocol $CD150^{v2}$); *n*=4 mice per group; **P*=0.0353. **j–n**, Frequency (% live) of CLPs (**j**), $IL7Ra^+$ cells (**k**), CMPs&GMPs (**l**), MkPs (**m**), and MEPs (**n**), after anti-CD150, anti-CD62p, or anti-NEO1 conditioning protocols. Values relative to mean of untreated control mice and log2-transformed; *n*=3 mice per group ($NEO1^{v1}$, $NEO1^{v2}$, $CD150^{v1}$); *n*=4 mice per group (CD62p, $CD150^{v2}$). **o**, Ratio of frequency (% live) for Lymphoid to Myeloid Progenitors (CLP)/(CMP&GMP), after anti-CD150, anti-CD62p, or anti-NEO1 antibody protocols. Values relative to mean of untreated control mice and log2-transformed; *n*=3 mice per group ($NEO1^{v1}$, $NEO1^{v2}$, $CD150^{v1}$); *n*=4 mice per group (CD62p, $CD150^{v2}$). **p**, Frequency (% live) of my-HSCs, bal-HSCs, $NEO1^+$ HSCs, and $NEO1^-$ HSCs after treatment with anti-CD150, anti-CD62p, or anti-NEO1 protocols; *n*=3 mice per group (anti-$CD150^{v1}$); *n*=4 mice per group (anti-CD62p); *n*=3 control mice and *n*=6 treated mice (anti-NEO1, combined 90ug&200ug protocols). Values relative to mean of control mice and log2-transformed. For **j–p**, values for treated mice (filled circles); values for control mice (unfilled circles). **q**, Correlation of fraction of live cells for my-HSCs vs. $NEO1^+$ HSCs (left), and bal-HSCs vs. $NEO1^-$ HSCs (right), of control mice and mice receiving anti-CD150, anti-CD62p, or anti-NEO1 protocols, in cKIT-enriched BM; *n*=3 mice (anti-$CD150^{v1}$); *n*=4 mice (anti-CD62p); *n*=3 control mice and *n*=6 treated mice (anti-NEO1, combined 90ug&200ug protocols). **r**, Comparison of the absolute number of cells in total (non-cKIT-enriched) BM (y-axis) vs. frequency of cells as a percent-live (in cKIT-enriched) BM (x-axis), for my-HSCs, bal-HSCs, CLP, CMP&GMP, and MkP in control mice and mice receiving anti-CD150, anti-CD150+anti-CD47, or anti-CD150+anti-CD47+anti-cKIT; *n*=3 mice per condition. **s**, Comparison of the frequency of cells as a fraction of total (non-cKIT-enriched) BM (x-axis) vs. the frequency of cells as a fraction of cKIT-enriched BM (y-axis), for cell populations in control mice and mice receiving anti-CD150, anti-CD150+anti-CD47, or anti-CD150+anti-CD47+anti-cKIT; *n*=3 mice per condition. Data for **q–s** log10-transformed. **t–v**, HSC lineage potential 8-weeks after transplantation of 100 total HSCs FACS-sorted from CD45.2 aged mice without (A) or with my-HSC depletion (A+C) into CD45.1 recipients. Donor Myeloid to Lymphoid Ratio (**t**, **P*=0.0275) and Percent-Chimerism Ratio (**u**, **P*=0.0340). For each recipient (y-axis), % donor cells (bottom x-axis) that are Myeloid (*red* bars) or Lymphoid (*blue* bars) and the Myeloid/Lymphoid log2-ratio (*red* circles) (top x-axis) (**v**); *n*=13 recipient mice (A), *n*=14 recipient mice (A+C). **w**, Donor Myeloid/Lymphoid Ratio 16-weeks after transplantation of 100 total HSCs FACS-sorted from CD45.2 aged mice without (A) or with my-HSC depletion (A+C) into CD45.1 recipients; *n*=12 recipient mice (A), *n*=14 recipient mice (A+C); **P*=0.0232. **x**, Top 200 differentially expressed genes ranked by p-value for RNA-seq comparison between (A) vs. (A+C), based on Fragments Per Kilobase of transcript per Million mapped reads (FPKM); log2-transformed. Heatmap generated using Phantasus[110] (v1.21.5) with FPKM values as input and Limma[112] to define differentially expressed genes;

n=3 mice (A), *n*=3 mice (A+C). Mouse ages approximately: 6-7 months (**a–d, r–s**), 7-9 months (**g–i**), 5-9 months (**j–q**), 11 months (donors, **t–w**), 2 months (recipients, **v**). For (**a, c, g–s**), BM was cKIT-enriched prior to analysis. For (**b**, **d**, **e–f**, **r–s**), total BM (non cKIT-enriched) was examined. *P*-values obtained by ordinary one-way ANOVA followed by one-tailed Dunnett's multiple comparisons test with non-treated as control (**a–d**), unpaired parametric one-tailed t-test (**i-k, p, t–u**), unpaired non-parametric one-tailed t-test (**w**), or unpaired parametric two-tailed t-test (**e–h, l–o**). *p*-values and R values calculated with one-tailed Pearson correlation coefficient (**q–s**). CD150^{v1} is rat IgG2b anti-CD150 protocol; CD150^{v2} is rat IgG2a anti-CD150 protocol; NEO1^{v2} includes mouse IgG2a anti-goat; α, anti-; ns, not significant. Bars indicate mean +/− s.e.m. *n* represents independent mice; **P*<0.05, ***P*<0.005, ****P*<0.0005; Exact *P*-values provided in Source Data.

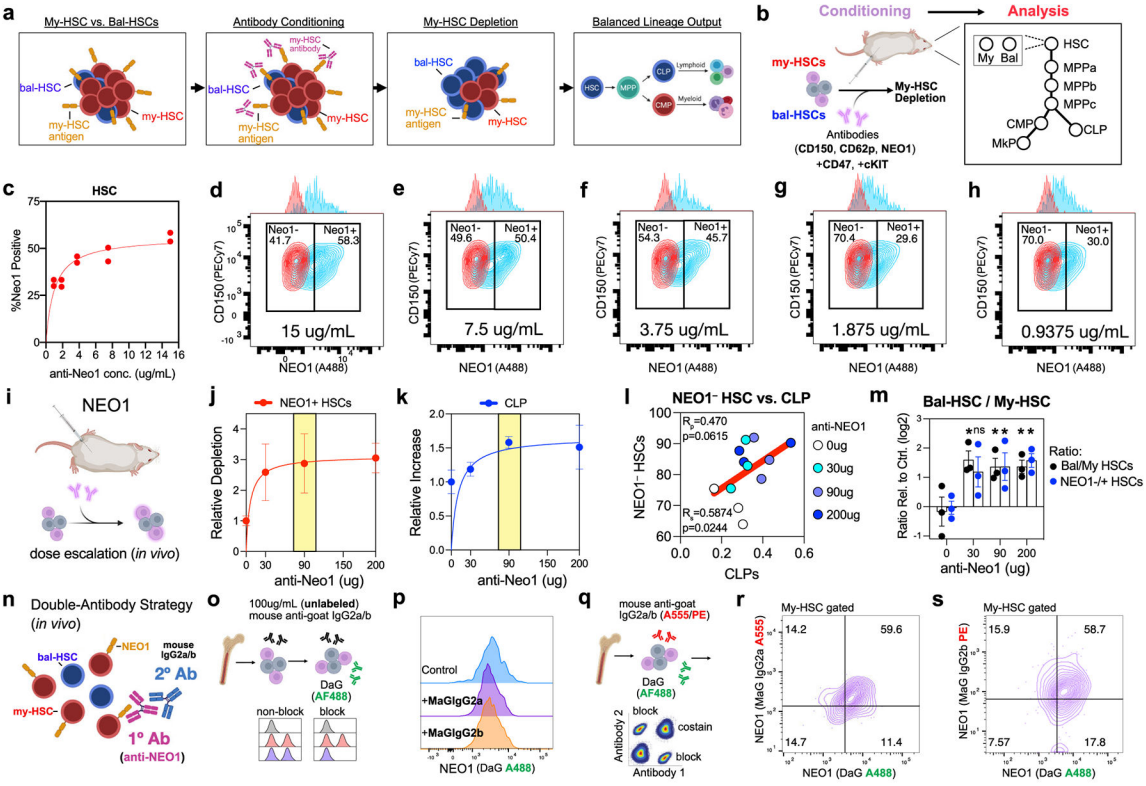

Extended Data Figure 5 l. Optimization of NEO1 depletion protocol *in vitro* and *in vivo*

a–b, Strategy to restore balanced lineage output by depleting my-HSCs. **c–h**, Anti-NEO1 antibody saturation curve (**c**) determined from *in vitro* antibody dilution series (**d–h**). **i**, Schematic of *in vivo* saturation experiments with anti-NEO1 antibody; used in panels **j–m**. **j–m**, Dose-dependent relationship between anti-NEO1 antibody dose (0ug, 30ug, 90ug, 200ug), when combined with anti-CD47 and anti-cKIT, on the relative depletion of NEO1^{+} HSCs (**j**), and increase in CLPs (**k**). Optimal concentration in yellow; *n*=3 mice per group. **l**, The increase in NEO1^{-} HSCs after anti-NEO1 dose escalation (0ug, 30ug, 90ug, 200ug) is correlated with the increase in CLPs. **m**, Impact on the ratio of Bal-HSCs/My-HSCs (*black*) and NEO1^{-}HSCs/NEO1^{+} HSCs (*blue*) as a percentage of live cells after anti-NEO1 antibody dose-escalation (0ug, 30ug, 90ug, 200ug), when combined

with anti-CD47 and anti-cKIT; *n*=3 per group. Values relative to mean value of control (0ug) mice and log2-transformed. **n**, Schematic of double-antibody strategy to target NEO1, whereby mouse IgG2a or IgG2b monoclonal anti-goat antibodies are administered 24 hours after goat anti-NEO1[93,94]. **o–p**, Schematic (**o**) to demonstrate that saturating concentrations of mouse IgG2a or IgG2b anti-goat do not reduce ability of donkey anti-goat AF488 detect goat anti-NEO1 antibody (**p**). **q–s**, Schematic (**q**) of experiment demonstrating that mouse anti-goat IgG2a A555 (**r**) and IgG2b PE (**s**) antibodies identify the same population as donkey anti-goat AF488 by flow-cytometry. Mouse ages approximately: 5-7 months (**c–h, n–s**), 6-9 months (**i–m**). For (**c–s**), BM was cKIT-enriched prior to analysis. For correlation *p*-values, one-tailed Pearson correlation coefficient (R_p), and one-tailed Spearman correlation coefficient (R_s) were calculated (**l**). *p*-values obtained by ordinary one-way ANOVA followed by one-tailed Dunnett's multiple comparisons test with 0ug condition as control (**m**). MaG, mouse-anti goat; DaG, donkey anti-goat. Bars indicate mean +/− s.e.m. *n* represents independent mice; **P*<0.05, ***P*<0.005, ****P*<0.0005; Exact *P*-values provided in Source Data.

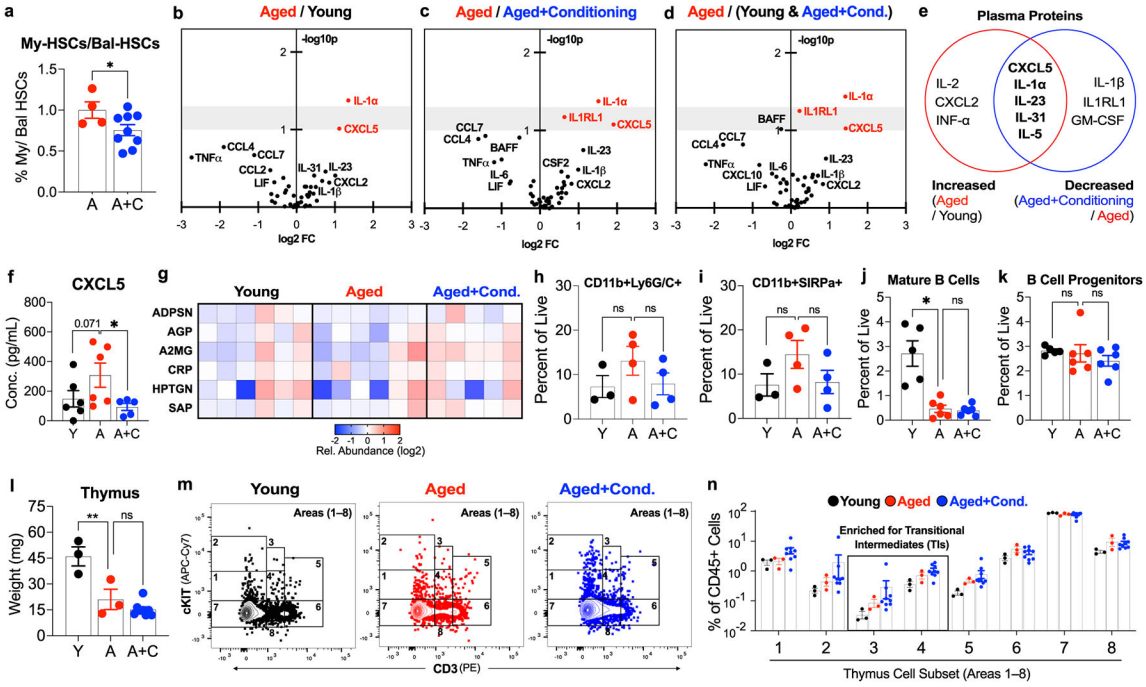

Extended Data Figure 6 l. My-HSC depletion restores features of a youthful immune system

a, Ratio of frequency of my-HSCs to bal-HSCs (% live) in aged (A), or aged+conditioning mice (A+C) after 8-weeks; *n*=4 (A), *n*=9 (A+C); *P*=0.0346. **b–d**, Statistical significance (y-axis, −log10p) vs. fold-change (x-axis, log2-FC) of plasma protein levels at week-8 for (A)/(Y) (**b**), (A)/(A+C) (**c**), or (A)/(Y & A+C) (**d**) comparisons. Gray bar (y=1–1.3); values above gray bar p<0.05; *n*=6 (Y, A), *n*=5 (A+C). **e**, Overlap of top 17% of plasma proteins, ranked by statistical significance, increased in (A)/(Y) and decreased in (A+C)/(A). **f**, Estimated plasma concentration of CXCL5[116] at week-8; *n*=6 (Y, A), *n*=5 (A+C). **g**, Relative plasma abundance of inflammatory proteins at week-8; *n*=6 (Y, A), *n*=5 (A+C). Values relative to the mean for (Y) and log2-transformed. **h–i**, Frequency of $CD11b^+Ly6G/C^+$

(**h**) and CD11b^{+}SIRPa^{+} (**i**) mature myeloid cells in the blood approximately 1-week after antibody-conditioning; n=3 (A), n=4 (A, A+C). **j–k**, Frequency of mature B cells (B220^{+}CD19^{+}CD43^{-}CD93^{-}IgM^{+}IgD^{+}) (**j**), and progenitor B cells (B220^{+}CD19^{-} B cells) (**k**), in the BM approximately 1-week after antibody-conditioning; n=5 (A), n=6 (A, A+C). Thymus weight (**l**) and frequency of thymic subsets 1–8 as defined by Akashi & Weissman[117], as % of total CD45^{+} cells in the thymus (**n**), 8-weeks after antibody-conditioning; representative FACS (**m**); n=3 (Y, A), n=9 (A+C). Populations enriched for transitional intermediate cells (areas 3&4) [117] highlighted in box (**n**). Mouse ages: Y (3-6 months); A & A+C (18-24 months). For (**a**), BM was cKIT-enriched prior to analysis. p-values obtained by unpaired parametric one-tailed t-test (**a**), ordinary one-way ANOVA followed by one-tailed Dunnett's multiple comparisons test using Aged as control (**f**), one-way ANOVA followed by Holm multiple comparisons test (**b–d**, **g**), ordinary one-way ANOVA followed by two-tailed Dunnett's multiple comparisons test using Aged as control (**h–i, l, n**), or Brown-Forsythe and Welch ANOVA tests followed by Dunnett's T3 multiple comparisons test using Aged as control (**j–k**). Bars indicate mean +/− s.e.m. n represents independent mice; *P<0.05, **P<0.005, ***P<0.0005; Exact P-values provided in Source Data.

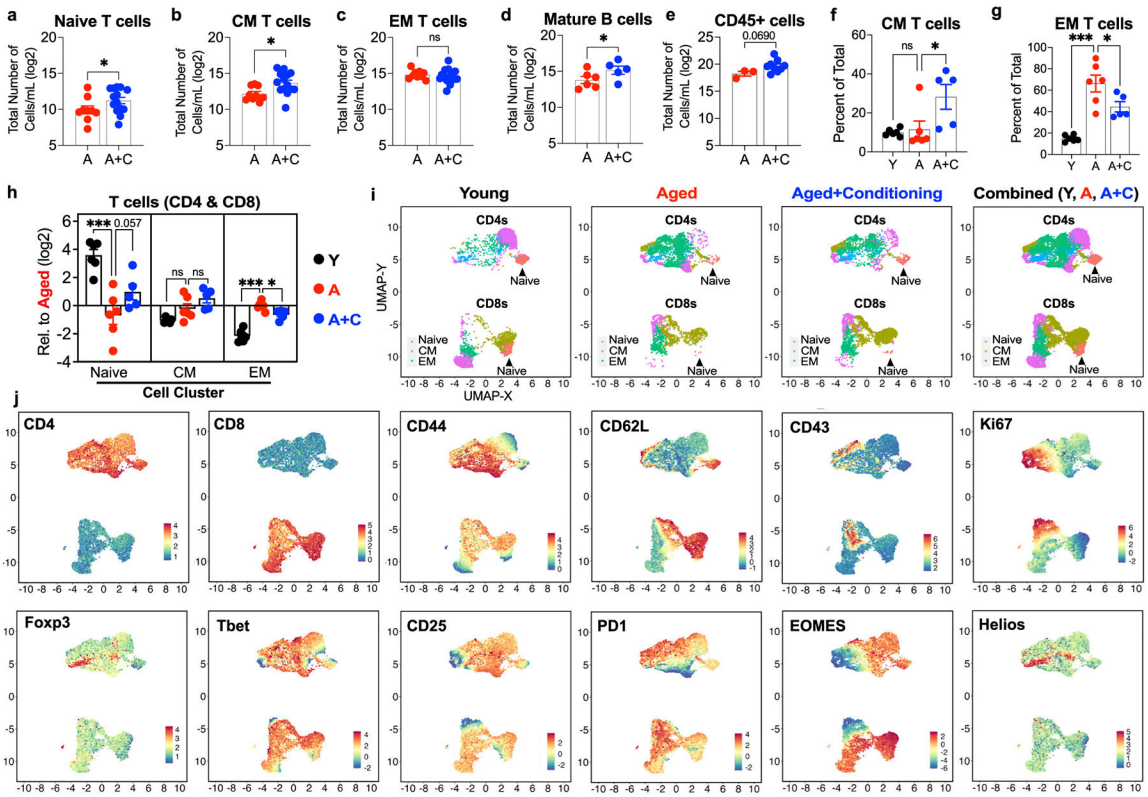

Extended Data Figure 7 | My-HSC depletion increases naïve T cells and B cells in aged mice

a–c, Absolute numbers of (**a**) naïve (CD44^{-}CD62L^{+}); *P=0.0430, (**b**) central memory (CM: CD44^{+}CD62L^{+}); *P=0.0177, or (**c**) effector memory (EM: CD44^{+}CD62L^{-}); P=0.576, T cells (CD4 & CD8), per mL of blood, approximately 8-weeks post-treatment. Values log2-transformed; n=9 (A), n=14 (A+C), mice pooled from 2 independent experiments. **d**,

Absolute numbers of mature B cells (IgM^+IgD^+) per mL of blood, approximately 8-weeks post-treatment; *P=0.0498. Values log2-transformed; n=6 (A), n=5 (A+C). **e**, Absolute numbers of CD45+ cells per mL of blood, approximately 8-weeks post-treatment. Values log2-transformed; n=3 (A), n=9 (A+C); P=0.069. **f–g**, Percentage of CM (**f**) and EM (**g**) subsets per total T cells (CD4 & CD8), 8-weeks post-treatment; n=6 (Y, A), n=5 (A+C). **h–j**, Frequency relative to Aged mice of T cell (CD4 & CD8) subsets 8-weeks after antibody treatment (**h**). Naïve, CM, and EM subsets were defined by 12-marker cluster-based analysis (**i–j**); n=6 (Y, A), n=5 (A+C). Values relative to mean for Aged control mice and log2-transformed. Mouse ages: Y (3-6 months); A & A+C (18-24 months). p-values obtained by unpaired parametric one-tailed t-test (**a**, **d**), unpaired parametric two-tailed t-test (**b–c**, **e**), or ordinary one-way ANOVA followed by two-tailed (**f–g**) or one-tailed (**h**) Dunnett's multiple comparisons test using Aged as control. Bars indicate mean +/− s.e.m. n represents independent mice; *P<0.05, **P<0.005, ***P<0.0005; Exact P-values provided in Source Data.

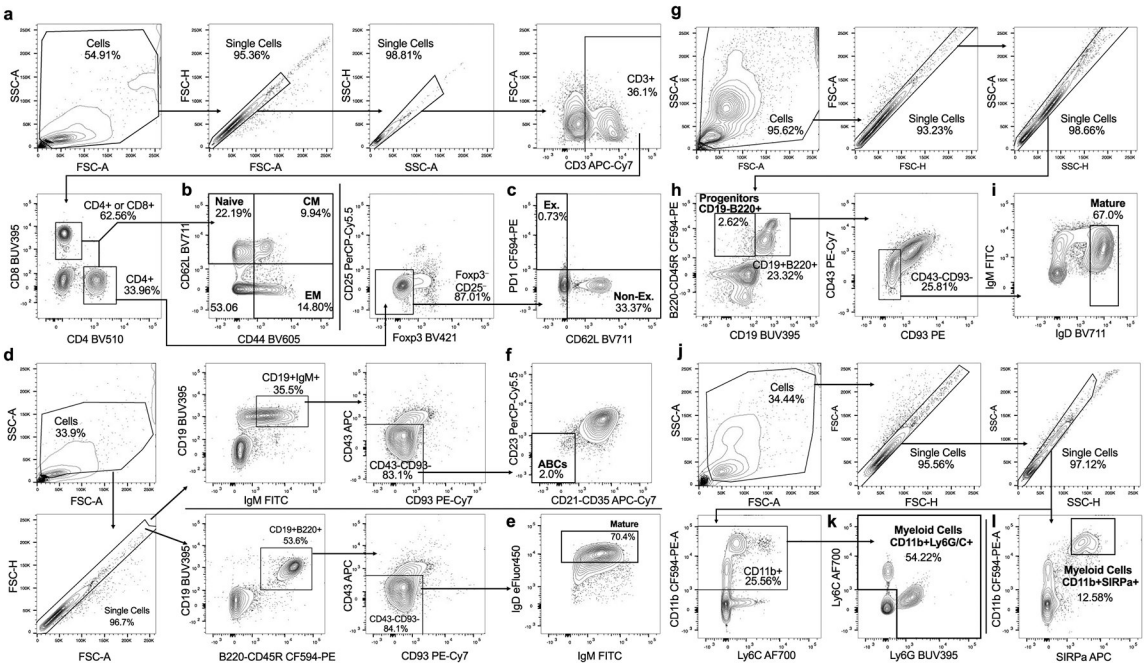

Extended Data Figure 8 |. Flow-cytometry gating strategy for T cells, B cells, and myeloid cells

a–c, Gating strategy to identify: (**b**) naïve ($CD44^-CD62L^+$), central memory ($CD44^+CD62L^+$), and effector memory ($CD44^+CD62L^-$) T cells (combined CD4 & CD8), or (**c**) CD4 T cells that are $PD1^+CD62L^-$ or $PD1^-CD62L^+$[41] in the blood, used for Fig. 3e, Fig. 3g, Extended Data Fig. 7a-c, Extended Data Fig. 7f-g. **d–f**, Gating strategy to identify: (**e**) mature B cells ($CD19^+B220^+IgM^+IgD^+$)[118], or (**f**) Aged B Cells ABCs[119] ($CD19^+IgM^+CD93^-CD43^-CD21/CD35^-CD23^-$)[42] in the blood, used for Fig. 3f, Fig. 3h, Extended Data Fig. 7d. **g–i**, Gating strategy to identify (**h**) progenitor B cells ($B220^+CD19^-$), or (**i**) mature B cells ($B220^+CD19^+CD43^-CD93^-IgM^+IgD^+$) in the bone-marrow, used for Extended Data Fig. 6j-k. **j–l**, Gating strategy to identify (**k**)

CD11b^{+}Ly6G/C^{+} myeloid cells, or (**l**) CD11b^{+}SIRPa^{+} myeloid cells in the blood, used for Extended Data Fig. 6h-i.

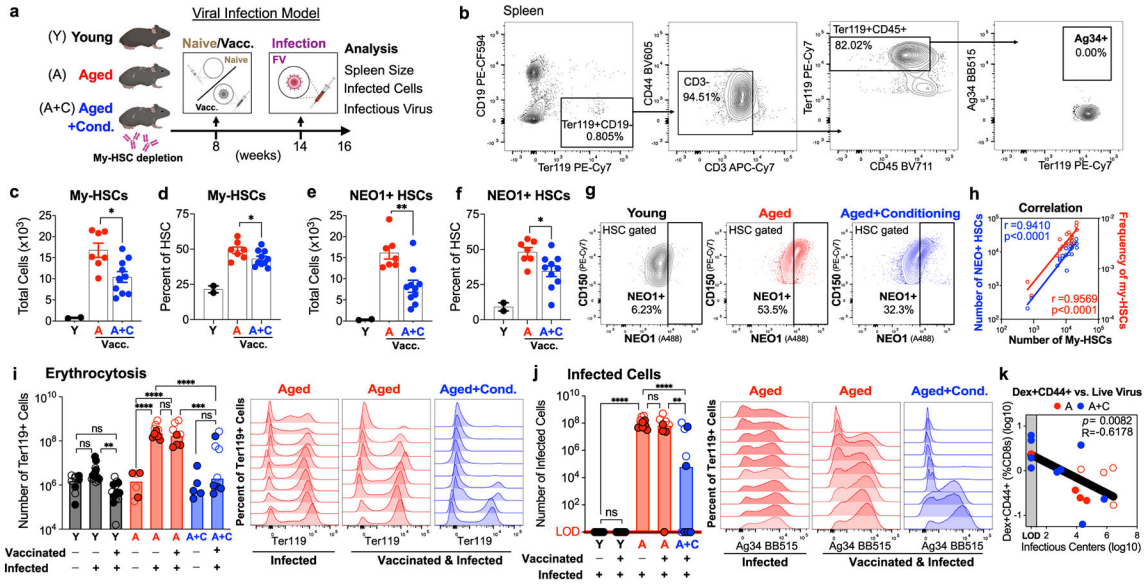

Extended Data Figure 9 |. Antibody-conditioning enhances functional immunity to infection

a, Schematic of model to determine the impact of antibody-conditioning on functional immunity. **b**, Gating to identify Ter119^{+} cells (Ter119^{+}CD19^{-}CD3^{-}CD45$^{+/lo}$) and antigen-infected cells (Ag34^{+}Ter119^{+}) in mouse spleens, used for Extended Data Fig. 9i-j. **c–h**, My-HSC and NEO1^{+} HSC absolute numbers in total BM (**c**, **e**), or as percentage of total HSCs (**d**, **f**), with correlations (**h**), 10-weeks after anti-NEO1^{v2} conditioning. Representative FACS on total HSCs (**g**). A and A+C mice received vaccination at Week 8; n=2 (Y), n=7 (A), n=10 (A+C). **i**, Total number of Ter119^{+} cells per mouse spleen in mice that were Naïve, Infected, or Vaccinated & Infected with FV. Representative FACS histograms for Ter119 expression, gated on all single cells. Each row represents an independent mouse. n=9 (Y, naïve), n=13 (Y, FV infected), n=13 (Y, vaccinated & FV infected), n=6 (A, naïve), n=10 (A, FV infected), n=8 (A, vaccinated & FV infected), n=5 (A+C, naïve), n=9 (A+C, vaccinated & FV infected). Data log10-transformed. **j**, Total number of antigen-infected (Ag34^{+}Ter119^{+}) cells per spleen in mice that were: Infected, or Vaccinated & Infected with FV. Representative FACS histograms for Ag34 expression, gated on Ter119+ cells. Each row represents an independent mouse; n=13 (Y, FV infected), n=13 (Y, vaccinated & FV infected), n=10 (A, FV infected), n=8 (A, vaccinated & FV infected), n=9 (A+C, vaccinated & FV infected). Data log10(x+1)-transformed. **k**, Correlation of Infectious virus levels (Infectious Centers; x-axis) vs. Dextramer^{+}CD44^{+} cells (Percent of splenic CD8+ T cells; y-axis) in Vaccinated & FV-infected mice; n=8 (A, vaccinated & FV-infected), n=9 (A+C, vaccinated & FV-infected). Data log10-transformed. For **i–k**, data from experiments using the anti-NEO1^{v1} protocol (open circles) or the anti-NEO1^{v2} protocol (closed circles) were combined. Mouse ages: Y (3-6 months); A & A+C (21-22 months). For (**c–f**), BM was cKIT-enriched prior to analysis. For (**c**, **e**, **h**), total BM (non-cKIT-enriched) was also analyzed to calculate total numbers of cells. p-values obtained by one-tailed unpaired

parametric t-test (**c–f**), two-tailed Pearson correlation coefficient (**h, k**), or ordinary one-way ANOVA followed by Tukey's multiple comparisons test (**i–j**). NEO1^{v2} protocol is NEO1^{v1} protocol (anti-NEO1+ anti-CD47+anti-cKIT)+mouse (IgG2a) anti-goat. Inf., FV infected without vaccination; Vacc. & Inf., FV infected with vaccination, Vacc. & Inf., FV infected with vaccination; LOD, limit of detection; n.s., not significant. *n* represents independent mice. Bars indicate mean +/− s.e.m. (**c–f**) or bars depict median (**i–j**). **P*<0.05, ***P*<0.005, ****P*<0.0005; Exact *P*-values provided in Source Data.

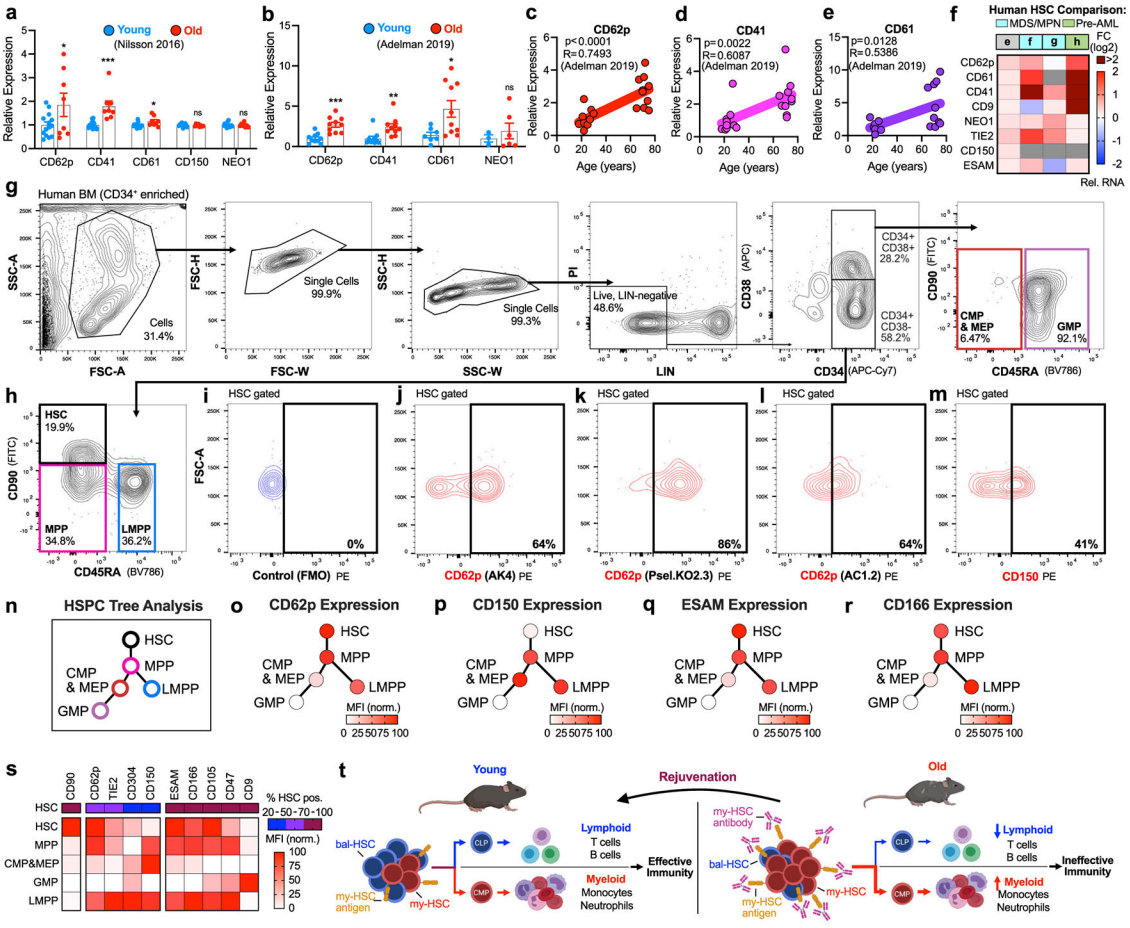

Extended Data Figure 10 | Mouse my-HSC markers are enriched in aged human HSCs

a, Relative mRNA expression of CD62p (*Selp*, *P*=0.0243), CD41 (*Itga2b*, *P*=0.0001), CD61 (*Itgb*3, *P*=0.0135), CD150 (*Slamf1*, *P*=0.179), and NEO1 (*Neo1*, *P*=0.433) in human HSCs isolated from young (age 20-26) and old (age >70) donors; data obtained from Nilsson[54], GSE69408. **b**, Relative mRNA expression of CD62p (*Selp*, *P*=0.0001), CD41 (*Itga2b*, *P*=0.0027), CD61 (*Itgb3*, *P*=0.0116), and NEO1 (*Neo1*, *P*=0.274) in human HSCs isolated from young (age 18-30) or old (age 65-75) donors; data obtained from Adelman[53] (GSE104406). **c–e**, Correlation of relative mRNA expression of CD62p (**c**), CD41 (**d**), and CD61 (**e**) in human HSCs as compared to donor age; data obtained from Adelman[53] (GSE104406). For **a–e**, values relative to mean of young samples. **f**, Heatmap depicting expression of candidate markers in independent

datasets of human: HMGA2$^+$ vs. HMGA2$^-$ CD34$^+$ cells (*e*[104]), MPN (*f*[56]) or MDS (*g*[57]) vs. normal HSCs, and Pre-AML vs. normal HSCs (*h*[58]). **g–h**, Representative FACS to identify human HSCs (Lin$^-$CD34$^+$CD38$^-$CD45RA$^-$CD90$^+$)[59], MPPs (Lin$^-$CD34$^+$CD38$^-$CD45RA$^-$CD90$^-$)[59], LMPPs (Lin$^-$CD34$^+$CD38$^-$CD45RA$^+$)[120], CMPs & MEPs (Lin$^-$CD34$^+$CD38$^+$CD45RA$^-$)[121], and GMPs (Lin$^-$CD34$^+$CD38$^+$CD45RA$^+$)[121] in normal human BM[59], used for Fig. 5f-i, Extended Data Fig. 10i-s. Samples are post CD34$^+$-enrichment. **i–m**, FACS of human HSCs depicting fluorescence-minus-one (FMO) control (**i**), anti-CD62p clone AK4 (**j**), anti-CD62p clone Psel.KO2.3 (**k**), anti-CD62p clone AC1.2 (**l**), and anti-CD150 (**m**); representative for n=3 donors (**j**); n=2 donors (**k–m**). **n**, Illustration of human Hematopoietic Stem and Progenitor Cell (HSPC) Tree Analysis (**n**). **o–s**, Relative expression of CD62p (**o**), CD150 (**p**), ESAM (**q**), and CD166 (**r**), on human HSPCs, with summary (**s**), showing percent positive HSCs, and normalized MFI for each marker on HSPCs. For **o–s**, FACS median fluorescent intensity (MFI) values for each marker were obtained for each population, divided by the MFI for the FMO control, and then normalized from 0–100 based on the lowest to highest expression. Red color scale corresponds to normalized MFI values. Blue, purple, maroon scale corresponds to bins for HSC positivity (20-50%, 51-70%, and 71-100). **t**, Model to rejuvenate aged immune systems by depleting myeloid-biased hematopoietic stem cells. *p*-values obtained by unpaired parametric one-tailed t-test (**a–b**), or *p*-values and R values calculated with one-tailed Pearson correlation coefficient (**c–e**). MDS, myelodysplastic syndrome; MPN, myeloproliferative neoplasms. Bars indicate mean +/− s.e.m. *P<0.05, **P<0.005, ***P<0.0005; Exact P-values provided in Source Data.

Supplementary Material

Refer to Web version on PubMed Central for supplementary material.

Acknowledgements

We thank members of the Weissman and Hasenkrug laboratories for advice and discussions. We thank A. McCarty, T. Naik, L. Quinn, and T. Raveh for technical and logistical support. We thank A. Banuelos, G. Blacker, B. George, G. Gulati, J. Liu, R. Sinha, M. Tal, N. Womack, and Y. Yiu for general help, advice, and experimental support. We thank C. Carswell-Crumpton, C. Pan, J. Pasillas, and the Stanford Institute for Stem Cell Biology and Regenerative Medicine FACS Core for flow cytometry assistance. We thank H. Maecker and I. Herschmann of the Stanford Human Immune Monitoring Center (HIMC) for assistance with immunoassays. We thank the Rocky Mountain Veterinary Branch (RMVB), especially T. Wiediger, for excellent care of the aged mice. This work was partially funded by the Intramural Research Program of the National Institute of Allergy and Infectious Diseases, National Institutes of Health, USA; the NIH/NCI Outstanding Investigator Award (R35CA220434 to I.L.W.); the NIH NIDDK (R01DK115600 to I.L.W.); the NIH NIAID (R01AI143889 to I.L.W.); and the Virginia and D.K. Ludwig Fund for Cancer Research (to I.L.W.). J.B.R was supported by the Stanford Radiation Oncology Kaplan Research Fellowship, the RSNA Resident/Fellow Research Grant, and the Stanford Cancer Institute Fellowship Award and the Ellie Guardino Research Fund. This work was supported by the Stanford Cancer Institute, an NCI-designated Comprehensive Cancer Center. J.J.N. was supported by Stanford University Medical Scientist Training Program grant T32-GM007365 and T32-GM145402. E.D. was supported by grants from NIH NIDDK (5T32DK098132-09 and 1TL1DK139565-01). The funders had no role in study design, data collection and analysis, decision to publish, or preparation of the manuscript. Some illustrations were created with BioRender.com.

Data Availability

Data for all graphical representations is provide in Source Data files. RNA-sequencing data has been deposited at Gene Expression Omnibus at GSE252062 and Sequence Read Archive

(SRA) with BioProject ID: PRJNA1054066. The following publicly available datasets were used: GSE43729[16], GSE39553[24], GSE48893[25], GSE109546[26], GSE27686[27], GSE44923[28], GSE128050[29], GSE47819[30], GSE130504[19], GSE112769[22], E-MEXP-3935[21], GSE32719[3], GSE104406[53], GSE69408[54], GSE115348[55], GSE107594[104], GSE111410[56], GSE55689[57], GSE74246[58], GSE132040[108], GSE87633[109], GSE100428[18].

References

1. Morrison SJ, Wandycz AM, Akashi K, Globerson A, and Weissman IL (1996). The aging of hematopoietic stem cells. Nat Med 2, 1011–1016. 10.1038/nm0996-1011. [PubMed: 8782459]
2. Rossi DJ, Jamieson CH, and Weissman IL (2008). Stems cells and the pathways to aging and cancer. Cell 132, 681–696. 10.1016/j.cell.2008.01.036. [PubMed: 18295583]
3. Pang WW, Price EA, Sahoo D, Beerman I, Maloney WJ, Rossi DJ, Schrier SL, and Weissman IL (2011). Human bone marrow hematopoietic stem cells are increased in frequency and myeloid-biased with age. Proc Natl Acad Sci U S A 108, 20012–20017. 10.1073/pnas.1116110108. [PubMed: 22123971]
4. Yamamoto R, and Nakauchi H (2020). In vivo clonal analysis of aging hematopoietic stem cells. Mechanisms of Ageing and Development 192, 111378. 10.1016/j.mad.2020.111378. [PubMed: 33022333]
5. Beerman I, Bhattacharya D, Zandi S, Sigvardsson M, Weissman IL, Bryder D, and Rossi DJ (2010). Functionally distinct hematopoietic stem cells modulate hematopoietic lineage potential during aging by a mechanism of clonal expansion. Proc Natl Acad Sci U S A 107, 5465–5470. 10.1073/pnas.1000834107. [PubMed: 20304793]
6. Rossi DJ, Bryder D, Zahn JM, Ahlenius H, Sonu R, Wagers AJ, and Weissman IL (2005). Cell intrinsic alterations underlie hematopoietic stem cell aging. Proc Natl Acad Sci U S A 102, 9194–9199. 10.1073/pnas.0503280102. [PubMed: 15967997]
7. Muller-Sieburg CE, Cho RH, Karlsson L, Huang JF, and Sieburg HB (2004). Myeloid-biased hematopoietic stem cells have extensive self-renewal capacity but generate diminished lymphoid progeny with impaired IL-7 responsiveness. Blood 103, 4111–4118. 10.1182/blood-2003-10-3448. [PubMed: 14976059]
8. Sudo K, Ema H, Morita Y, and Nakauchi H (2000). Age-associated characteristics of murine hematopoietic stem cells. J Exp Med 192, 1273–1280. 10.1084/jem.192.9.1273. [PubMed: 11067876]
9. Sieburg HB, Cho RH, Dykstra B, Uchida N, Eaves CJ, and Muller-Sieburg CE (2006). The hematopoietic stem compartment consists of a limited number of discrete stem cell subsets. Blood 107, 2311–2316. 10.1182/blood-2005-07-2970. [PubMed: 16291588]
10. Dykstra B, Kent D, Bowie M, McCaffrey L, Hamilton M, Lyons K, Lee S-J, Brinkman R, and Eaves C (2007). Long-Term Propagation of Distinct Hematopoietic Differentiation Programs In Vivo. Cell Stem Cell 1, 218–229. 10.1016/j.stem.2007.05.015. [PubMed: 18371352]
11. Dykstra B, Olthof S, Schreuder J, Ritsema M, and de Haan G (2011). Clonal analysis reveals multiple functional defects of aged murine hematopoietic stem cells. J Exp Med 208, 2691–2703. 10.1084/jem.20111490. [PubMed: 22110168]
12. Min H, Montecino-Rodriguez E, and Dorshkind K (2006). Effects of aging on the common lymphoid progenitor to pro-B cell transition. J Immunol 176, 1007–1012. 10.4049/jimmunol.176.2.1007. [PubMed: 16393987]
13. Montecino-Rodriguez E, Berent-Maoz B, and Dorshkind K (2013). Causes, consequences, and reversal of immune system aging. J Clin Invest 123, 958–965. 10.1172/JCI64096. [PubMed: 23454758]
14. Yang D, and de Haan G (2021). Inflammation and Aging of Hematopoietic Stem Cells in Their Niche. Cells 10. 10.3390/cells10081849.
15. Chen JY, Miyanishi M, Wang SK, Yamazaki S, Sinha R, Kao KS, Seita J, Sahoo D, Nakauchi H, and Weissman IL (2016). Hoxb5 marks long-term haematopoietic stem cells and

reveals a homogenous perivascular niche. Nature 530, 223–227. 10.1038/nature16943. [PubMed: 26863982]

16. Beerman I, Bock C, Brian Zachary, Gu H, Meissner A, and Derrick (2013). Proliferation-Dependent Alterations of the DNA Methylation Landscape Underlie Hematopoietic Stem Cell Aging. Cell Stem Cell 12, 413–425. 10.1016/j.stem.2013.01.017. [PubMed: 23415915]
17. Gekas C, and Graf T (2013). CD41 expression marks myeloid-biased adult hematopoietic stem cells and increases with age. Blood 121, 4463–4472. 10.1182/blood-2012-09-457929. [PubMed: 23564910]
18. Mann M, Mehta A, De Boer CG, Kowalczyk MS, Lee K, Haldeman P, Rogel N, Knecht AR, Farouq D, Regev A, and Baltimore D (2018). Heterogeneous Responses of Hematopoietic Stem Cells to Inflammatory Stimuli Are Altered with Age. Cell Reports 25, 2992–3005.e2995. 10.1016/j.celrep.2018.11.056. [PubMed: 30540934]
19. Gulati GS, Zukowska M, Noh JJ, Zhang A, Wesche DJ, Sinha R, George BM, Weissman IL, and Szade K (2019). Neogenin-1 distinguishes between myeloid-biased and balanced. Proc Natl Acad Sci U S A 116, 25115–25125. 10.1073/pnas.1911024116. [PubMed: 31754028]
20. Flohr Svendsen A, Yang D, Kim K, Lazare S, Skinder N, Zwart E, Mura-Meszaros A, Ausema A, Von Eyss B, De Haan G, and Bystrykh L (2021). A comprehensive transcriptome signature of murine hematopoietic stem cell aging. Blood 138, 439–451. 10.1182/blood.2020009729. [PubMed: 33876187]
21. Sanjuan-Pla A, Macaulay IC, Jensen CT, Woll PS, Luis TC, Mead A, Moore S, Carella C, Matsuoka S, Bouriez Jones T, et al. (2013). Platelet-biased stem cells reside at the apex of the haematopoietic stem-cell hierarchy. Nature 502, 232–236. 10.1038/nature12495. [PubMed: 23934107]
22. Montecino-Rodriguez E, Kong Y, Casero D, Rouault A, Dorshkind K, and Pioli PD (2019). Lymphoid-Biased Hematopoietic Stem Cells Are Maintained with Age and Efficiently Generate Lymphoid Progeny. Stem Cell Reports 12, 584–596. 10.1016/j.stemcr.2019.01.016. [PubMed: 30799276]
23. Zaro BW, Noh JJ, Mascetti VL, Demeter J, George B, Zukowska M, Gulati GS, Sinha R, Flynn RA, Banuelos A, et al. (2020). Proteomic analysis of young and old mouse hematopoietic stem cells and their progenitors reveals post-transcriptional regulation in stem cells. Elife 9. 10.7554/eLife.62210.
24. Bersenev A, Rozenova K, Balcerek J, Jiang J, Wu C, and Tong W (2012). Lnk deficiency partially mitigates hematopoietic stem cell aging. Aging Cell 11, 949–959. 10.1111/j.1474-9726.2012.00862.x. [PubMed: 22812478]
25. Flach J, Bakker ST, Mohrin M, Conroy PC, Pietras EM, Reynaud D, Alvarez S, Diolaiti ME, Ugarte F, Forsberg EC, et al. (2014). Replication stress is a potent driver of functional decline in ageing haematopoietic stem cells. Nature 512, 198–202. 10.1038/nature13619. [PubMed: 25079315]
26. Maryanovich M, Zahalka AH, Pierce H, Pinho S, Nakahara F, Asada N, Wei Q, Wang X, Ciero P, Xu J, et al. (2018). Adrenergic nerve degeneration in bone marrow drives aging of the hematopoietic stem cell niche. Nat Med 24, 782–791. 10.1038/s41591-018-0030-x. [PubMed: 29736022]
27. Norddahl GL, Pronk CJ, Wahlestedt M, Sten G, Nygren JM, Ugale A, Sigvardsson M, and Bryder D (2011). Accumulating mitochondrial DNA mutations drive premature hematopoietic aging phenotypes distinct from physiological stem cell aging. Cell Stem Cell 8, 499–510. 10.1016/j.stem.2011.03.009. [PubMed: 21549326]
28. Wahlestedt M, Norddahl GL, Sten G, Ugale A, Frisk MA, Mattsson R, Deierborg T, Sigvardsson M, and Bryder D (2013). An epigenetic component of hematopoietic stem cell aging amenable to reprogramming into a young state. Blood 121, 4257–4264. 10.1182/blood-2012-11-469080. [PubMed: 23476050]
29. Renders S, Svendsen AF, Panten J, Rama N, Maryanovich M, Sommerkamp P, Ladel L, Redavid AR, Gibert B, Lazare S, et al. (2021). Niche derived netrin-1 regulates hematopoietic stem cell dormancy via its receptor neogenin-1. Nat Commun 12, 608. 10.1038/s41467-020-20801-0. [PubMed: 33504783]

30. Sun D, Luo M, Jeong M, Rodriguez B, Xia Z, Hannah R, Wang H, Le T, Faull KF, Chen R, et al. (2014). Epigenomic profiling of young and aged HSCs reveals concerted changes during aging that reinforce self-renewal. Cell Stem Cell 14, 673–688. 10.1016/j.stem.2014.03.002. [PubMed: 24792119]

31. Seita J, Sahoo D, Rossi DJ, Bhattacharya D, Serwold T, Inlay MA, Ehrlich LI, Fathman JW, Dill DL, and Weissman IL (2012). Gene Expression Commons: an open platform for absolute gene expression profiling. PLoS One 7, e40321. 10.1371/journal.pone.0040321. [PubMed: 22815738]

32. Akashi K, Traver D, Miyamoto T, and Weissman IL (2000). A clonogenic common myeloid progenitor that gives rise to all myeloid lineages. Nature 404, 193–197. 10.1038/35004599. [PubMed: 10724173]

33. Kondo M, Weissman IL, and Akashi K (1997). Identification of clonogenic common lymphoid progenitors in mouse bone marrow. Cell 91, 661–672. 10.1016/s0092-8674(00)80453-5. [PubMed: 9393859]

34. George BM, Kao KS, Kwon HS, Velasco BJ, Poyser J, Chen A, Le AC, Chhabra A, Burnett CE, Cajuste D, et al. (2019). Antibody Conditioning Enables MHC-Mismatched Hematopoietic Stem Cell Transplants and Organ Graft Tolerance. Cell Stem Cell 25, 185–192.e183. 10.1016/j.stem.2019.05.018. [PubMed: 31204177]

35. Czechowicz A, Kraft D, Weissman IL, and Bhattacharya D (2007). Efficient transplantation via antibody-based clearance of hematopoietic stem cell niches. Science 318, 1296–1299. 10.1126/science.1149726. [PubMed: 18033883]

36. Jaiswal S, Jamieson CH, Pang WW, Park CY, Chao MP, Majeti R, Traver D, van Rooijen N, and Weissman IL (2009). CD47 is upregulated on circulating hematopoietic stem cells and leukemia cells to avoid phagocytosis. Cell 138, 271–285. 10.1016/j.cell.2009.05.046. [PubMed: 19632178]

37. Kuribayashi W, Oshima M, Itokawa N, Koide S, Nakajima-Takagi Y, Yamashita M, Yamazaki S, Rahmutulla B, Miura F, Ito T, et al. (2021). Limited rejuvenation of aged hematopoietic stem cells in young bone marrow niche. J Exp Med 218. 10.1084/jem.20192283.

38. Morrison SJ, and Weissman IL (1994). The long-term repopulating subset of hematopoietic stem cells is deterministic and isolatable by phenotype. Immunity 1, 661–673. 10.1016/1074-7613(94)90037-x. [PubMed: 7541305]

39. Akashi K, Kondo M, and Weissman IL (1998). Two distinct pathways of positive selection for thymocytes. Proc Natl Acad Sci U S A 95, 2486–2491. 10.1073/pnas.95.5.2486. [PubMed: 9482912]

40. Gattinoni L, Lugli E, Ji Y, Pos Z, Paulos CM, Quigley MF, Almeida JR, Gostick E, Yu Z, Carpenito C, et al. (2011). A human memory T cell subset with stem cell-like properties. Nat Med 17, 1290–1297. 10.1038/nm.2446. [PubMed: 21926977]

41. Elyahu Y, Hekselman I, Eizenberg-Magar I, Berner O, Strominger I, Schiller M, Mittal K, Nemirovsky A, Eremenko E, Vital A, et al. (2019). Aging promotes reorganization of the CD4 T cell landscape toward extreme regulatory and effector phenotypes. Sci Adv 5, eaaw8330. 10.1126/sciadv.aaw8330. [PubMed: 31457092]

42. Hao Y, O'Neill P, Naradikian MS, Scholz JL, and Cancro MP (2011). A B-cell subset uniquely responsive to innate stimuli accumulates in aged mice. Blood 118, 1294–1304. 10.1182/blood-2011-01-330530. [PubMed: 21562046]

43. Pioli PD, Casero D, Montecino-Rodriguez E, Morrison SL, and Dorshkind K (2019). Plasma Cells Are Obligate Effectors of Enhanced Myelopoiesis in Aging Bone Marrow. Immunity 51, 351–366.e356. 10.1016/j.immuni.2019.06.006. [PubMed: 31303400]

44. Kovtonyuk LV, Caiado F, Garcia-Martin S, Manz EM, Helbling P, Takizawa H, Boettcher S, Al-Shahrour F, Nombela-Arrieta C, Slack E, and Manz MG (2022). IL-1 mediates microbiome-induced inflammaging of hematopoietic stem cells in mice. Blood 139, 44–58. 10.1182/blood.2021011570. [PubMed: 34525198]

45. Collier DA, Ferreira IATM, Kotagiri P, Datir RP, Lim EY, Touizer E, Meng B, Abdullahi A, Elmer A, Kingston N, et al. (2021). Age-related immune response heterogeneity to SARS-CoV-2 vaccine BNT162b2. Nature 596, 417–422. 10.1038/s41586-021-03739-1. [PubMed: 34192737]

46. Myers L, and Hasenkrug KJ (2009). Retroviral immunology: lessons from a mouse model. Immunol Res 43, 160–166. 10.1007/s12026-008-8061-x. [PubMed: 18830572]

47. Dittmer U, Sutter K, Kassiotis G, Zelinskyy G, Bánki Z, Stoiber H, Santiago ML, and Hasenkrug KJ (2019). Friend retrovirus studies reveal complex interactions between intrinsic, innate and adaptive immunity. FEMS Microbiol Rev 43, 435–456. 10.1093/femsre/fuz012. [PubMed: 31087035]
48. Dittmer U, Brooks DM, and Hasenkrug KJ (1999). Requirement for multiple lymphocyte subsets in protection by a live attenuated vaccine against retroviral infection. Nat Med 5, 189–193. 10.1038/5550. [PubMed: 9930867]
49. Dittmer U, Brooks DM, and Hasenkrug KJ (1998). Characterization of a live-attenuated retroviral vaccine demonstrates protection via immune mechanisms. J Virol 72, 6554–6558. 10.1128/JVI.72.8.6554-6558.1998. [PubMed: 9658099]
50. Dittmer U, Brooks DM, and Hasenkrug KJ (1999). Protection against establishment of retroviral persistence by vaccination with a live attenuated virus. J Virol 73, 3753–3757. 10.1128/JVI.73.5.3753-3757.1999. [PubMed: 10196269]
51. Hasenkrug KJ, and Dittmer U (2000). The role of CD4 and CD8 T cells in recovery and protection from retroviral infection: lessons from the Friend virus model. Virology 272, 244–249. 10.1006/viro.2000.0387. [PubMed: 10873767]
52. Larochelle A, Savona M, Wiggins M, Anderson S, Ichwan B, Keyvanfar K, Morrison SJ, and Dunbar CE (2011). Human and rhesus macaque hematopoietic stem cells cannot be purified based only on SLAM family markers. Blood 117, 1550–1554. 10.1182/blood-2009-03-212803. [PubMed: 21163926]
53. Adelman ER, Huang HT, Roisman A, Olsson A, Colaprico A, Qin T, Lindsley RC, Bejar R, Salomonis N, Grimes HL, and Figueroa ME (2019). Aging Human Hematopoietic Stem Cells Manifest Profound Epigenetic Reprogramming of Enhancers That May Predispose to Leukemia. Cancer Discov 9, 1080–1101. 10.1158/2159-8290.CD-18-1474. [PubMed: 31085557]
54. Rundberg Nilsson A, Soneji S, Adolfsson S, Bryder D, and Pronk CJ (2016). Human and Murine Hematopoietic Stem Cell Aging Is Associated with Functional Impairments and Intrinsic Megakaryocytic/Erythroid Bias. PLoS One 11, e0158369. 10.1371/journal.pone.0158369. [PubMed: 27368054]
55. Hennrich ML, Romanov N, Horn P, Jaeger S, Eckstein V, Steeples V, Ye F, Ding X, Poisa-Beiro L, Lai MC, et al. (2018). Cell-specific proteome analyses of human bone marrow reveal molecular features of age-dependent functional decline. Nat Commun 9, 4004. 10.1038/s41467-018-06353-4. [PubMed: 30275468]
56. Tong J, Sun T, Ma S, Zhao Y, Ju M, Gao Y, Zhu P, Tan P, Fu R, Zhang A, et al. (2021). Hematopoietic stem cell heterogeneity is linked to the initiation and therapeutic response of myeloproliferative neoplasms. Cell Stem Cell 28, 780. 10.1016/j.stem.2021.02.026. [PubMed: 33798424]
57. Woll PS, Kjällquist U, Chowdhury O, Doolittle H, Wedge DC, Thongjuea S, Erlandsson R, Ngara M, Anderson K, Deng Q, et al. (2014). Myelodysplastic syndromes are propagated by rare and distinct human cancer stem cells in vivo. Cancer Cell 25, 794–808. 10.1016/j.ccr.2014.03.036. [PubMed: 24835589]
58. Corces MR, Buenrostro JD, Wu B, Greenside PG, Chan SM, Koenig JL, Snyder MP, Pritchard JK, Kundaje A, Greenleaf WJ, et al. (2016). Lineage-specific and single-cell chromatin accessibility charts human hematopoiesis and leukemia evolution. Nat Genet 48, 1193–1203. 10.1038/ng.3646. [PubMed: 27526324]
59. Merad M, Blish CA, Sallusto F, and Iwasaki A (2022). The immunology and immunopathology of COVID-19. Science 375, 1122–1127. 10.1126/science.abm8108. [PubMed: 35271343]
60. Hirata Y, Furuhashi K, Ishii H, Li HW, Pinho S, Ding L, Robson SC, Frenette PS, and Fujisaki J (2018). CD150high bone marrow Tregs maintain hematopoietic stem cell quiescence and immune privilege via adenosine. Cell stem cell 22, 445–453. e445. [PubMed: 29456159]
61. Busque L, Patel JP, Figueroa ME, Vasanthakumar A, Provost S, Hamilou Z, Mollica L, Li J, Viale A, Heguy A, et al. (2012). Recurrent somatic TET2 mutations in normal elderly individuals with clonal hematopoiesis. Nat Genet 44, 1179–1181. 10.1038/ng.2413. [PubMed: 23001125]
62. Jan M, Snyder TM, Corces-Zimmerman MR, Vyas P, Weissman IL, Quake SR, and Majeti R (2012). Clonal evolution of preleukemic hematopoietic stem cells precedes human acute myeloid leukemia. Sci Transl Med 4, 149ra118. 10.1126/scitranslmed.3004315.

63. Jamieson CHM, and Weissman IL (2023). Stem-Cell Aging and Pathways to Precancer Evolution. N Engl J Med 389, 1310–1319. 10.1056/NEJMra2304431. [PubMed: 37792614]
64. Jaiswal S, and Ebert BL (2019). Clonal hematopoiesis in human aging and disease. Science 366. 10.1126/science.aan4673.
65. Jaiswal S, Natarajan P, Silver AJ, Gibson CJ, Bick AG, Shvartz E, McConkey M, Gupta N, Gabriel S, Ardissino D, et al. (2017). Clonal Hematopoiesis and Risk of Atherosclerotic Cardiovascular Disease. N Engl J Med 377, 111–121. 10.1056/NEJMoa1701719. [PubMed: 28636844]
66. Majeti R, Jamieson C, Pang WW, Jaiswal S, Leeper NJ, Wernig G, and Weissman IL (2022). Clonal Expansion of Stem/Progenitor Cells in Cancer, Fibrotic Diseases, and Atherosclerosis, and CD47 Protection of Pathogenic Cells. Annu Rev Med 73, 307–320. 10.1146/annurev-med-042420-104436. [PubMed: 35084991]
67. Park CY, Majeti R, and Weissman IL (2008). In vivo evaluation of human hematopoiesis through xenotransplantation of purified hematopoietic stem cells from umbilical cord blood. Nat Protoc 3, 1932–1940. 10.1038/nprot.2008.194. [PubMed: 19180077]
68. Bhattacharya D, Cheah MT, Franco CB, Hosen N, Pin CL, Sha WC, and Weissman IL (2007). Transcriptional profiling of antigen-dependent murine B cell differentiation and memory formation. J Immunol 179, 6808–6819. 10.4049/jimmunol.179.10.6808. [PubMed: 17982071]
69. Luckey CJ, Bhattacharya D, Goldrath AW, Weissman IL, Benoist C, and Mathis D (2006). Memory T and memory B cells share a transcriptional program of self-renewal with long-term hematopoietic stem cells. Proc Natl Acad Sci U S A 103, 3304–3309. 10.1073/pnas.0511137103. [PubMed: 16492737]
70. Saggau C, Martini GR, Rosati E, Meise S, Messner B, Kamps AK, Bekel N, Gigla J, Rose R, Voß M, et al. (2022). The pre-exposure SARS-CoV-2-specific T cell repertoire determines the quality of the immune response to vaccination. Immunity. 10.1016/j.immuni.2022.08.003.
71. Jaiswal S, and Weissman IL (2009). Hematopoietic stem and progenitor cells and the inflammatory response. Ann N Y Acad Sci 1174, 118–121. 10.1111/j.1749-6632.2009.04930.x. [PubMed: 19769744]
72. Spangrude GJ, Heimfeld S, and Weissman IL (1988). Purification and characterization of mouse hematopoietic stem cells. Science 241, 58–62. 10.1126/science.2898810. [PubMed: 2898810]
73. Osawa M, Hanada K, Hamada H, and Nakauchi H (1996). Long-term lymphohematopoietic reconstitution by a single CD34-low/negative hematopoietic stem cell. Science 273, 242–245. 10.1126/science.273.5272.242. [PubMed: 8662508]
74. Smith LG, Weissman IL, and Heimfeld S (1991). Clonal analysis of hematopoietic stem-cell differentiation in vivo. Proc Natl Acad Sci U S A 88, 2788–2792. 10.1073/pnas.88.7.2788. [PubMed: 1672767]
75. Yamamoto R, Wilkinson AC, Ooehara J, Lan X, Lai CY, Nakauchi Y, Pritchard JK, and Nakauchi H (2018). Large-Scale Clonal Analysis Resolves Aging of the Mouse Hematopoietic Stem Cell Compartment. Cell Stem Cell 22, 600–607.e604. 10.1016/j.stem.2018.03.013. [PubMed: 29625072]
76. Myers LM, Tal MC, Torrez Dulgeroff LB, Carmody AB, Messer RJ, Gulati G, Yiu YY, Staron MM, Angel CL, and Sinha R (2019). A functional subset of CD8+ T cells during chronic exhaustion is defined by SIRPα expression. Nature communications 10, 794.
77. Chesebro B, Wehrly K, Cloyd M, Britt W, Portis J, Collins J, and Nishio J (1981). Characterization of mouse monoclonal antibodies specific for Friend murine leukemia virus-induced erythroleukemia cells: friend-specific and FMR-specific antigens. Virology 112, 131–144. 10.1016/0042-6822(81)90619-x. [PubMed: 6787798]
78. Marsh-Wakefield FM, Mitchell AJ, Norton SE, Ashhurst TM, Leman JK, Roberts JM, Harte JE, McGuire HM, and Kemp RA (2021). Making the most of high-dimensional cytometry data. Immunol Cell Biol 99, 680–696. 10.1111/imcb.12456. [PubMed: 33797774]
79. Liechti T, Weber LM, Ashhurst TM, Stanley N, Prlic M, Van Gassen S, and Mair F (2021). An updated guide for the perplexed: cytometry in the high-dimensional era. Nat Immunol 22, 1190–1197. 10.1038/s41590-021-01006-z. [PubMed: 34489590]

80. Ashhurst TM, Marsh-Wakefield F, Putri GH, Spiteri AG, Shinko D, Read MN, Smith AL, and King NJC (2022). Integration, exploration, and analysis of high-dimensional single-cell cytometry data using Spectre. Cytometry A 101, 237–253. 10.1002/cyto.a.24350. [PubMed: 33840138]
81. Levine JH, Simonds EF, Bendall SC, Davis KL, Amir e.-A., Tadmor MD, Litvin O, Fienberg HG, Jager A, Zunder ER, et al. (2015). Data-Driven Phenotypic Dissection of AML Reveals Progenitor-like Cells that Correlate with Prognosis. Cell 162, 184–197. 10.1016/j.cell.2015.05.047. [PubMed: 26095251]
82. McInnes L, Healy J, and Melville J (2018). Umap: Uniform manifold approximation and projection for dimension reduction. arXiv preprint arXiv:1802.03426.
83. Baum CM, Weissman IL, Tsukamoto AS, Buckle AM, and Peault B (1992). Isolation of a candidate human hematopoietic stem-cell population. Proc Natl Acad Sci U S A 89, 28042808. 10.1073/pnas.89.7.2804.
84. Yiu YY, Hansen PS, Torrez Dulgeroff LB, Blacker G, Myers L, Galloway S, Gars E, Colace O, Mansfield P, Hasenkrug KJ, et al. (2022). CD47 Blockade Leads to Chemokine-Dependent Monocyte Infiltration and Loss of B Cells from the Splenic Marginal Zone. J Immunol 208, 1371–1377. 10.4049/jimmunol.2100352. [PubMed: 35236754]
85. Brignani S, Raj DDA, Schmidt ERE, Düdükcü Ö, Adolfs Y, De Ruiter AA, Rybiczka-Tesulov M, Verhagen MG, van der Meer C, Broekhoven MH, et al. (2020). Remotely Produced and Axon-Derived Netrin-1 Instructs GABAergic Neuron Migration and Dopaminergic Substantia Nigra Development. Neuron 107, 684–702.e689. 10.1016/j.neuron.2020.05.037. [PubMed: 32562661]
86. Hadi T, Boytard L, Silvestro M, Alebrahim D, Jacob S, Feinstein J, Barone K, Spiro W, Hutchison S, Simon R, et al. (2018). Macrophage-derived netrin-1 promotes abdominal aortic aneurysm formation by activating MMP3 in vascular smooth muscle cells. Nat Commun 9, 5022. 10.1038/s41467-018-07495-1. [PubMed: 30479344]
87. König K, Gatidou D, Granja T, Meier J, Rosenberger P, and Mirakaj V (2012). The axonal guidance receptor neogenin promotes acute inflammation. PLoS One 7, e32145. 10.1371/journal.pone.0032145. [PubMed: 22412855]
88. Li N, Liu H, Xue Y, Chen J, Kong X, and Zhang Y (2022). Upregulation of Neogenin-1 by a CREB1-BAF47 Complex in Vascular Endothelial Cells is Implicated in Atherogenesis. Front Cell Dev Biol 10, 803029. 10.3389/fcell.2022.803029. [PubMed: 35186922]
89. Robinson RA, Griffiths SC, van de Haar LL, Malinauskas T, van Battum EY, Zelina P, Schwab RA, Karia D, Malinauskaite L, Brignani S, et al. (2021). Simultaneous binding of Guidance Cues NET1 and RGM blocks extracellular NEO1 signaling. Cell 184, 2103–2120.e2131. 10.1016/j.cell.2021.02.045. [PubMed: 33740419]
90. Schlegel M, Granja T, Kaiser S, Körner A, Henes J, König K, Straub A, Rosenberger P, and Mirakaj V (2014). Inhibition of neogenin dampens hepatic ischemia-reperfusion injury. Crit Care Med 42, e610–619. 10.1097/CCM.0000000000000485. [PubMed: 25029243]
91. Schlegel M, Körner A, Kaussen T, Knausberg U, Gerber C, Hansmann G, Jónasdóttir HS, Giera M, and Mirakaj V (2019). Inhibition of neogenin fosters resolution of inflammation and tissue regeneration. J Clin Invest 129, 2165. 10.1172/JCI128681. [PubMed: 31042165]
92. van den Heuvel DM, Hellemons AJ, and Pasterkamp RJ (2013). Spatiotemporal expression of repulsive guidance molecules (RGMs) and their receptor neogenin in the mouse brain. PLoS One 8, e55828. 10.1371/journal.pone.0055828. [PubMed: 23457482]
93. Keren Z, Naor S, Nussbaum S, Golan K, Itkin T, Sasaki Y, Schmidt-Supprian M, Lapidot T, and Melamed D (2011). B-cell depletion reactivates B lymphopoiesis in the BM and rejuvenates the B lineage in aging. Blood 117, 3104–3112. 10.1182/blood-2010-09-307983. [PubMed: 21228330]
94. Säwén P, Lang S, Mandal P, Rossi DJ, Soneji S, and Bryder D (2016). Mitotic History Reveals Distinct Stem Cell Populations and Their Contributions to Hematopoiesis. Cell Rep 14, 2809–2818. 10.1016/j.celrep.2016.02.073. [PubMed: 26997272]
95. Boivin G, Faget J, Ancey PB, Gkasti A, Mussard J, Engblom C, Pfirschke C, Contat C, Pascual J, Vazquez J, et al. (2020). Durable and controlled depletion of neutrophils in mice. Nat Commun 11, 2762. 10.1038/s41467-020-16596-9. [PubMed: 32488020]

96. Chhabra A, Ring AM, Weiskopf K, Schnorr PJ, Gordon S, Le AC, Kwon HS, Ring NG, Volkmer J, Ho PY, et al. (2016). Hematopoietic stem cell transplantation in immunocompetent hosts without radiation or chemotherapy. Sci Transl Med 8, 351ra105. 10.1126/scitranslmed.aae0501.

97. Iglewicz B, and Hoaglin DC (1993). How to detect and handle outliers (Asq Press).

98. Council, N.R. (2010). Guide for the care and use of laboratory animals.

99. Robertson SJ, Ammann CG, Messer RJ, Carmody AB, Myers L, Dittmer U, Nair S, Gerlach N, Evans LH, Cafruny WA, and Hasenkrug KJ (2008). Suppression of acute anti-friend virus CD8+ T-cell responses by coinfection with lactate dehydrogenase-elevating virus. J Virol 82, 408–418. 10.1128/JVI.01413-07. [PubMed: 17959678]

100. Chesebro B, Wehrly K, and Stimpfling J (1974). Host genetic control of recovery from Friend leukemia virus-induced splenomegaly: mapping of a gene within the major histocompatability complex. J Exp Med 140, 1457–1467. 10.1084/jem.140.6.1457. [PubMed: 4430891]

101. Lander MR, and Chattopadhyay SK (1984). A Mus dunni cell line that lacks sequences closely related to endogenous murine leukemia viruses and can be infected by ectropic, amphotropic, xenotropic, and mink cell focus-forming viruses. J Virol 52, 695–698. 10.1128/JVI.52.2.695-698.1984. [PubMed: 6092693]

102. Robertson MN, Miyazawa M, Mori S, Caughey B, Evans LH, Hayes SF, and Chesebro B (1991). Production of monoclonal antibodies reactive with a denatured form of the Friend murine leukemia virus gp70 envelope protein: use in a focal infectivity assay, immunohistochemical studies, electron microscopy and western blotting. J Virol Methods 34, 255–271. 10.1016/0166-0934(91)90105-9. [PubMed: 1744218]

103. Horton H, Thomas EP, Stucky JA, Frank I, Moodie Z, Huang Y, Chiu YL, McElrath MJ, and De Rosa SC (2007). Optimization and validation of an 8-color intracellular cytokine staining (ICS) assay to quantify antigen-specific T cells induced by vaccination. J Immunol Methods 323, 39–54. 10.1016/j.jim.2007.03.002. [PubMed: 17451739]

104. Kumar P, Beck D, Galeev R, Thoms JAI, Talkhoncheh MS, de Jong I, Unnikrishnan A, Baudet A, Subramaniam A, Pimanda JE, and Larsson J (2019). HMGA2 promotes long-term engraftment and myeloerythroid differentiation of human hematopoietic stem and progenitor cells. Blood Adv 3, 681–691. 10.1182/bloodadvances.2018023986. [PubMed: 30808686]

105. Mahi NA, Najafabadi MF, Pilarczyk M, Kouril M, and Medvedovic M (2019). GREIN: An Interactive Web Platform for Re-analyzing GEO RNA-seq Data. Sci Rep 9, 7580. 10.1038/s41598-019-43935-8. [PubMed: 31110304]

106. Barrett T, Wilhite SE, Ledoux P, Evangelista C, Kim IF, Tomashevsky M, Marshall KA, Phillippy KH, Sherman PM, Holko M, et al. (2013). NCBI GEO: archive for functional genomics data sets--update. Nucleic Acids Res 41, D991–995. 10.1093/nar/gks1193. [PubMed: 23193258]

107. Edgar R, Domrachev M, and Lash AE (2002). Gene Expression Omnibus: NCBI gene expression and hybridization array data repository. Nucleic Acids Res 30, 207–210. 10.1093/nar/30.1.207. [PubMed: 11752295]

108. Consortium, T.M., coordination, O., coordination, L., processing, O.c.a., sequencing, L.p.a., analysis, C.d., annotation, C.t., group, W., group, S.t.w., and investigators, P. (2018). Single-cell transcriptomics of 20 mouse organs creates a Tabula Muris. Nature 562, 367–372. 10.1038/s41586-018-0590-4. [PubMed: 30283141]

109. Kadoki M, Patil A, Thaiss CC, Brooks DJ, Pandey S, Deep D, Alvarez D, von Andrian UH, Wagers AJ, Nakai K, et al. (2017). Organism-Level Analysis of Vaccination Reveals Networks of Protection across Tissues. Cell 171, 398–413.e321. 10.1016/j.cell.2017.08.024. [PubMed: 28942919]

110. Kleverov M, Zenkova D, Kamenev V, Sablina M, Artyomov MN, and Sergushichev AA (2022). Phantasus: web-application for visual and interactive gene expression analysis. bioRxiv, 2022.2012.2010.519861. 10.1101/2022.12.10.519861.

111. Love MI, Huber W, and Anders S (2014). Moderated estimation of fold change and dispersion for RNA-seq data with DESeq2. Genome Biol 15, 550. 10.1186/s13059-014-0550-8. [PubMed: 25516281]

112. Ritchie ME, Phipson B, Wu D, Hu Y, Law CW, Shi W, and Smyth GK (2015). limma powers differential expression analyses for RNA-sequencing and microarray studies. Nucleic Acids Res 43, e47. 10.1093/nar/gkv007. [PubMed: 25605792]
113. Subramanian A, Tamayo P, Mootha VK, Mukherjee S, Ebert BL, Gillette MA, Paulovich A, Pomeroy SL, Golub TR, Lander ES, and Mesirov JP (2005). Gene set enrichment analysis: a knowledge-based approach for interpreting genome-wide expression profiles. Proc Natl Acad Sci U S A 102, 15545–15550. 10.1073/pnas.0506580102. [PubMed: 16199517]
114. Liao Y, Wang J, Jaehnig EJ, Shi Z, and Zhang B (2019). WebGestalt 2019: gene set analysis toolkit with revamped UIs and APIs. Nucleic Acids Res 47, W199–W205. 10.1093/nar/gkz401. [PubMed: 31114916]
115. Seita J, and Weissman IL (2010). Hematopoietic stem cell: self-renewal versus differentiation. Wiley Interdiscip Rev Syst Biol Med 2, 640–653. 10.1002/wsbm.86. [PubMed: 20890962]
116. Helbling PM, Piñeiro-Yáñez E, Gerosa R, Boettcher S, Al-Shahrour F, Manz MG, and Nombela-Arrieta C (2019). Global Transcriptomic Profiling of the Bone Marrow Stromal Microenvironment during Postnatal Development, Aging, and Inflammation. Cell Rep 29, 3313–3330.e3314. 10.1016/j.celrep.2019.11.004. [PubMed: 31801092]
117. Akashi K, and Weissman IL (1996). The c-kit+ maturation pathway in mouse thymic T cell development: lineages and selection. Immunity 5, 147–161. 10.1016/s1074-7613(00)80491-4. [PubMed: 8769478]
118. Loder F, Mutschler B, Ray RJ, Paige CJ, Sideras P, Torres R, Lamers MC, and Carsetti R (1999). B cell development in the spleen takes place in discrete steps and is determined by the quality of B cell receptor-derived signals. J Exp Med 190, 75–89. 10.1084/jem.190.1.75. [PubMed: 10429672]
119. Leins H, Mulaw M, Eiwen K, Sakk V, Liang Y, Denkinger M, Geiger H, and Schirmbeck R (2018). Aged murine hematopoietic stem cells drive aging-associated immune remodeling. Blood 132, 565–576. 10.1182/blood-2018-02-831065. [PubMed: 29891535]
120. Goardon N, Marchi E, Atzberger A, Quek L, Schuh A, Soneji S, Woll P, Mead A, Alford KA, Rout R, et al. (2011). Coexistence of LMPP-like and GMP-like leukemia stem cells in acute myeloid leukemia. Cancer Cell 19, 138–152. 10.1016/j.ccr.2010.12.012. [PubMed: 21251617]
121. Manz MG, Miyamoto T, Akashi K, and Weissman IL (2002). Prospective isolation of human clonogenic common myeloid progenitors. Proc Natl Acad Sci U S A 99, 11872–11877. 10.1073/pnas.172384399. [PubMed: 12193648]

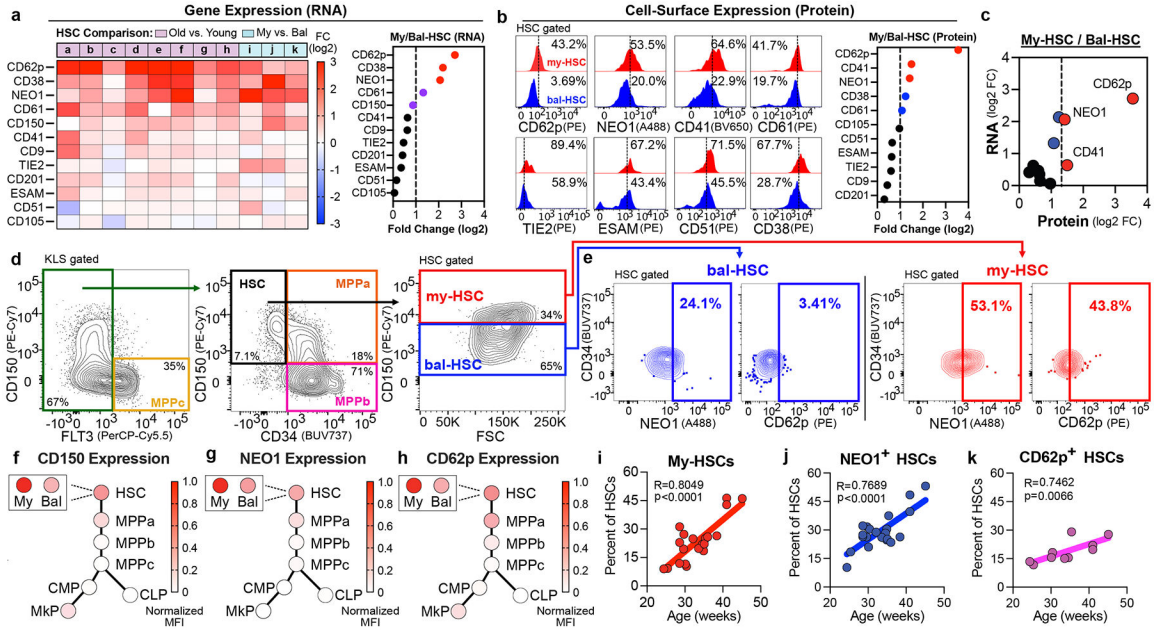

Figure 1 | Identification of cell-surface antigens on myeloid-biased HSCs

a, Heatmap depicting candidate marker expression across independent datasets (left), with mean log2 fold-change (Old-HSC vs. Young-HSC; My-HSC vs. Bal-HSC) (right). Datasets: Old vs. Young HSCs (*a*[16], *b*[24], *c*[25], *d*[26], *e*[27], *f*[28], *g*[29], *h*[30]) and My-HSCs vs. Bal-HSC (*i*[19], *j*[22], *k*[21]). **b**, Percent-positive for each marker on my-HSCs vs. bal-HSCs (left); plot of my-HSC fold-enrichment for each marker (right). **c**, Plot of (my-HSC)/(bal-HSC) Fold-Change (log2) of RNA expression (y-axis) vs. Cell-surface Protein expression (x-axis) for candidate markers. **d**, Representative flow-cytometry to identify total HSCs (KLS FLT3$^-$CD34$^-$CD150$^+$), my-HSCs (KLS FLT3$^-$CD34$^-$CD150^{High}), and bal-HSCs (KLS FLT3$^-$CD34$^-$CD150^{Low}) from mouse bone-marrow, after excluding dead cells, doublets, and gated on KLS (Lin$^-$cKIT$^+$Sca1$^+$). **e**, Representative flow-cytometry of percent of bal-HSCs (left) or my-HSCs (right) that are NEO1$^+$ or CD62p$^+$. **f–h**, Relative cell-surface expression of CD150 (**f**), NEO1 (**g**), and CD62p (**h**), on total HSC (my-HSC+bal-HSC), my-HSC, bal-HSC, MPPa, MPPb, MPPc, CMP (CMP&GMP), MkP, and CLP. Flow-cytometry median fluorescent intensity (MFI) for antibodies to each marker were obtained for each population and normalized from 0–1 (from lowest to highest). **i–k**, Percentage of total HSCs (KLS FLT3$^-$CD34$^-$CD150$^+$) that are my-HSCs (e.g., CD150^{High}) (**i**), NEO1$^+$ (**j**), or CD62p$^+$ (**k**) on the y-axis, vs. mouse age (weeks) on the x-axis; *n*=21 mice (**i–j**); *n*=10 mice (**k**). Mouse ages approximately: 4-6 months (**b–h**), 6-12 months (**i–k**). For (**b–k**), BM was cKIT-enriched prior to analysis. *p*-values and R values calculated with one-tailed Pearson correlation coefficient (**i–k**). *n* indicates independent mice. FC, fold-change.

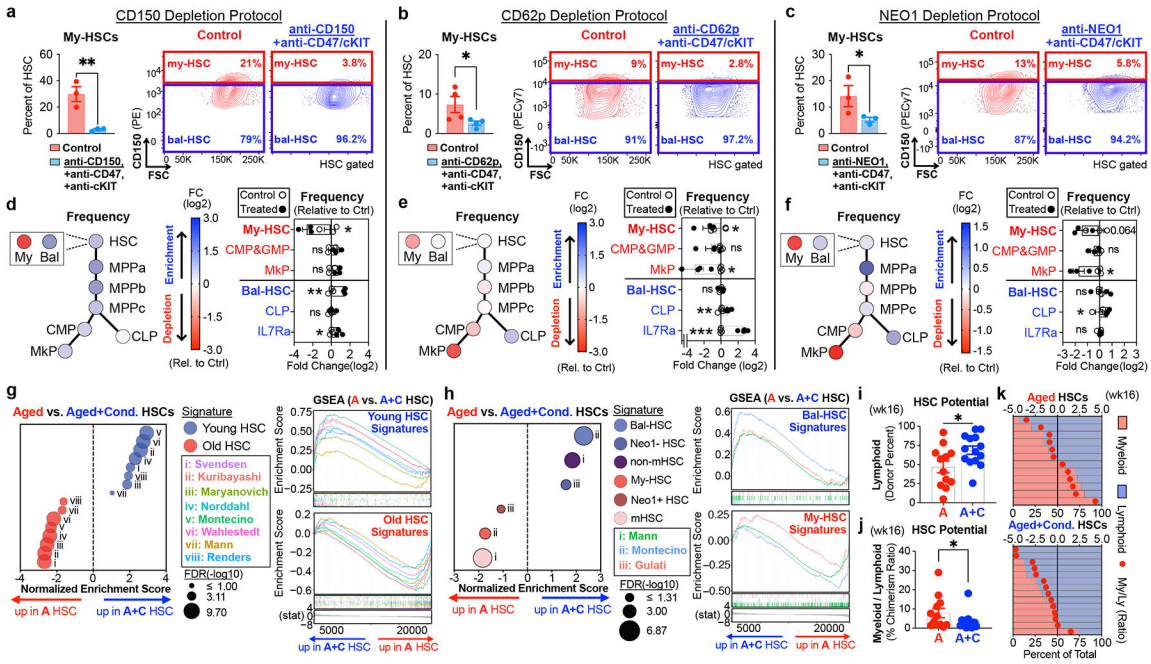

Figure 2 | Antibody-mediated depletion of my-HSCs *in vivo*

a–c, Percentage of Total HSCs that are my-HSCs after: anti-CD150 (**a**, ***P*=0.0045), anti-CD62p (**b**, **P*=0.0374), or anti-NEO1 (**c**, **P*=0.0465) optimized protocols (e.g., +anti-CD47+anti-cKIT), with representative flow-cytometry; *n*=3 mice per group (**a**, **c**); *n*=4 mice per group (**b**). **d–f**, Enrichment (*blue*) or depletion (*red*) as percent-live for Total HSCs (HSC), my-HSCs (My), bal-HSCs (Bal), MPPs, CLP, CMP&GMP, MkP after: anti-CD150 (**d**), anti-CD62p (**e**), or anti-NEO1 (**f**) protocols (+anti-CD47+anti-cKIT). Treated values relative to Control mean and log2-transformed; *n*=3 mice per group (**d**, **f**); *n*=4 mice per group (**e**). **g–k**, Total HSCs were FACS-sorted from aged mice without (Aged, A) or with my-HSC depletion (Aged+Conditioning, A+C) and underwent RNA-sequencing (**g–h**) or transplantation (**i–k**). Depletion was anti-NEO1+anti-CD62p+anti-CD47+anti-cKIT; *n*=3 mice (A), *n*=3 mice (A+C). **g–h**, GSEA comparison between (A) vs. (A+C) HSCs using gene-signatures from Young HSC vs. Old HSC (**g**[18,20,22,26-29,37]) or bal-HSC vs. my-HSC (**h**[18,19,22]); *n*=3 mice (A), *n*=3 mice (A+C). **i–k**, HSC lineage potential 16-weeks after transplantation of 100 total HSCs FACS-sorted from CD45.2 aged mice without (A) or with my-HSC depletion (A+C) into CD45.1 recipients. Donor Lymphoid Percentage (**i**, **P*=0.0126) and Myeloid/Lymphoid Percent-Chimerism Ratio (**j**, **P*=0.0492). For each recipient (y-axis), % donor cells (bottom x-axis) that are Myeloid (*red* bars) or Lymphoid (*blue* bars) and the Myeloid/Lymphoid log2-ratio (*red* circles) (top x-axis) (**k**); *n*=12 recipient mice (A), *n*=14 recipient mice (A+C). Mouse ages 5-9 months (**a–f**), 11 months (donors, **g–k**), 2 months (recipients, **i–k**). For (**a–k**) BM was cKIT-enriched prior to analysis or sorting. *P*-values obtained by unpaired parametric one-tailed t-test (**a–f**, **i–j**) or GSEA with FDR adjustment (**g–h**). Bars indicate mean +/− s.e.m. *n* indicates independent mice; **P*<0.05, ***P*<0.005, ****P*<0.0005; Exact *P*-values provided in Source Data.

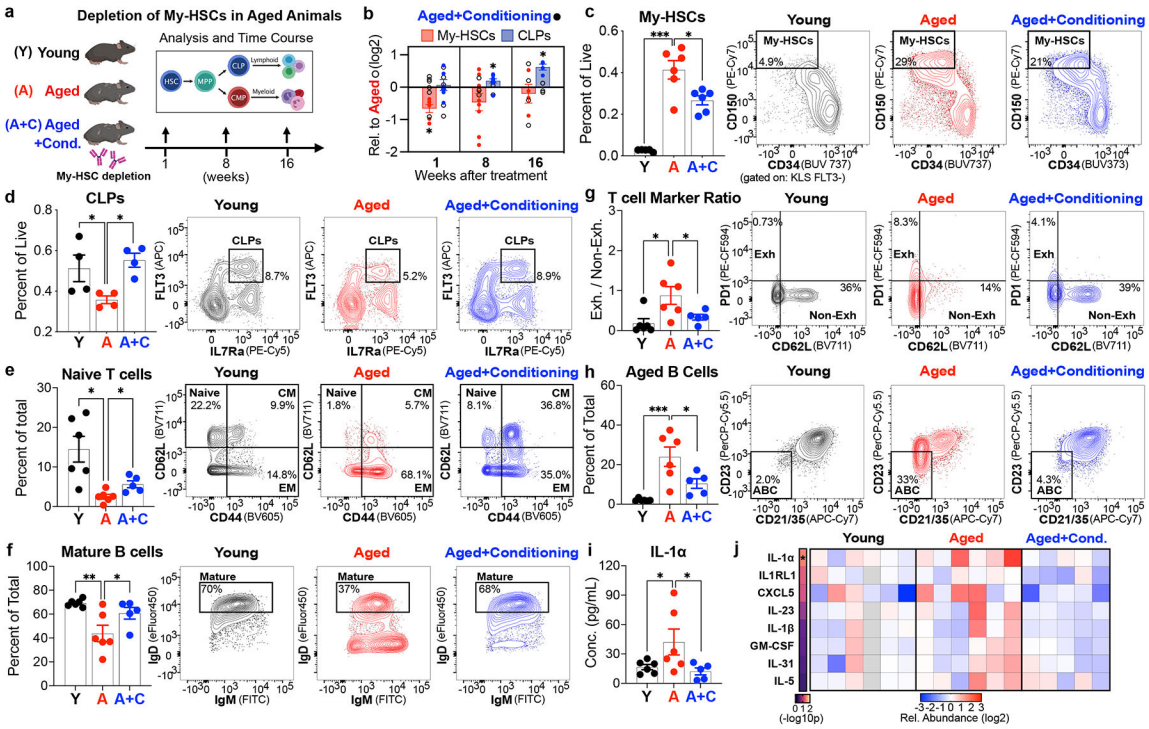

Figure 3 | Depletion of my-HSCs in aged mice restores youthful immune features

a, Young-adult mice (Y) compared to aged mice without (A), or with anti-NEO1 conditioning (A+C), approximately 1-, 8-, or 16-weeks post-treatment. **b**, Frequency (% live) of my-HSCs and CLPs in (A+C) relative to (A); n=6 (A, A+C) at 1-week; n=4 (A), n=9 (A+C) at 8-weeks; n=4 (A, A+C) at 16-weeks. Treated (A+C) values relative to mean of aged control (A) and log2-transformed. **c**, Frequency of my-HSCs (%-live) in BM at week-1; n=5 (Y), n=6 (A, A+C). **d**, Frequency of CLPs (%-live) in BM at week-16; n=4 (Y, A, A+C). **e–j**, Naïve T cells ($CD44^{-}CD62L^{+}$) as percent total CD4 & CD8 T cells in blood (**e**), Mature B cells ($IgM^{+}IgD^{+}$) as percent total B cells ($CD19^{+}B220^{+}$) in blood (**f**), CD4 T cell ratio (% $PD1^{+}CD62L^{-}$)/(% $PD1^{-}CD62L^{+}$)[41] (**g**), Aged B Cells (CD21/$CD35^{-}CD23^{-}$)[42] as percent total mature B cells ($CD19^{+}IgM^{+}CD93^{-}CD43^{-}$) in blood (**h**), plasma concentration of IL-1α (**i**), plasma abundance of top 17% proteins increased in (A) vs. (A+C) (**j**); for (**e–j**), data at week-8 and n=6 (Y, A), n=5 (A+C). For **j**, values relative to Young (Y) mean and log2-transformed; gray squares are removed statistical outliers; significance $-\log_{10}$p between (A) vs. (A+C). Mouse ages (**b–j**) approximately: young-adult (3-6 months), aged (18-24 months). For (**b–d**) BM was cKIT-enriched prior to analysis. p-values obtained by unpaired parametric one-tailed t-test (**b**), ordinary one-way ANOVA followed by one-tailed Dunnett's multiple comparison test using Aged as control (**c–d, f–i**), Brown-Forsythe and Welch ANOVA followed by two-tailed Dunnett's T3 multiple comparisons test using Aged as control (**e**), or one-way ANOVA followed by Holm multiple comparisons test (**j**). Bars indicate mean +/− s.e.m. n represents independent mice; *P<0.05, **P<0.005, ***P<0.0005; Exact P-values provided in Source Data.

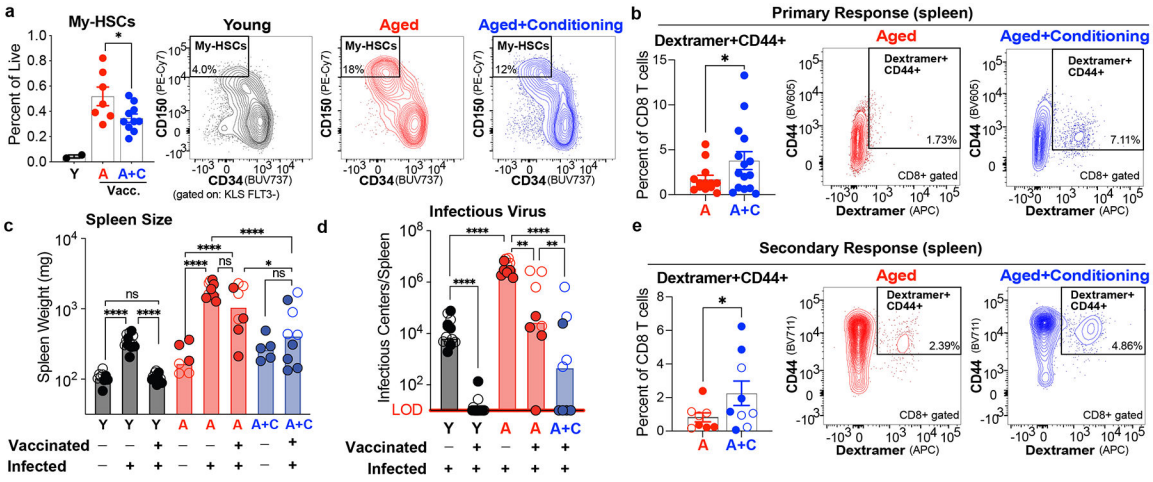

Figure 4 |. Antibody-conditioning enhances functional immunity in aged mice

a, Frequency of my-HSCs in young-adult (Y) or aged mice without (A), or with aged+conditioning (A+C), 10-weeks after anti-NEO1^{v2}; (A) and (A+C) mice were vaccinated 2-weeks before analysis; n=2 (Y), n=7 (A), n=10 (A+C); (A) vs. (A+C) *P=0.0159. **b**, Percentage of Dextramer^{+}CD44^{+} splenic CD8+ T cells 10-14 days after vaccination in aged-matched (20-26 months) mice without (A), or with antibody-conditioning (A+C). For (A+C), my-HSC-depletion was with anti-NEO1^{v2} 2-months before vaccination; n=13 (A, vaccinated), n=15 (A+C, vaccinated); *P=0.0412. **c,** Spleen weight (mg) for naïve, FV-infected, or Vaccinated & FV-infected mice; n=9 (Y, naïve), n=13 (Y, FV-infected), n=13 (Y, vaccinated & FV-infected), n=6 (A, naïve), n=10 (A, FV-infected), n=8 (A, vaccinated & FV-infected), n=5 (A+C, naïve), n=9 (A+C, vaccinated & FV-infected). Data log10-transformed. **d**, Infectious virus levels in FV-infected or Vaccinated & FV-infected mice; n=13 (Y, FV-infected), n=13 (Y, vaccinated & FV-infected), n=10 (A, FV-infected), n=8 (A, vaccinated & FV-infected), n=9 (A+C, vaccinated & FV-infected). Data log10-transformed. **e**, Percent of Dextramer^{+}CD44^{+} splenic CD8+ T cells in Vaccinated & FV-infected mice; n=8 (A, vaccinated & FV-infected), n=9 (A+C, vaccinated & FV-infected); *P=0.0473. For **a, c–e**, mouse ages approximately: (Y) 3-6 months; (A) & (A+C) 21-22 months. For **c–e**, data from experiments with anti-NEO1^{v1} (open circles) or anti-NEO1^{v2} (closed circles) were combined. For (**a**) BM was cKIT-enriched prior to analysis. p-values obtained by one-tailed unpaired parametric t-test (**a–b**), ordinary one-way ANOVA followed by Tukey's multiple comparisons test (**c–d**), or one-tailed unpaired parametric t-test with Welch's correction (**e**). anti-NEO1^{v2} is anti-NEO1^{v1} (anti-NEO1+anti-CD47+anti-cKIT)+mouse (IgG2a) anti-goat. Bars depict mean +/− s.e.m. (**a–b, e**) or bars depict median (**c–d**). n represents independent mice; *P<0.05, **P<0.005, ***P<0.0005; Exact P-values provided in Source Data.

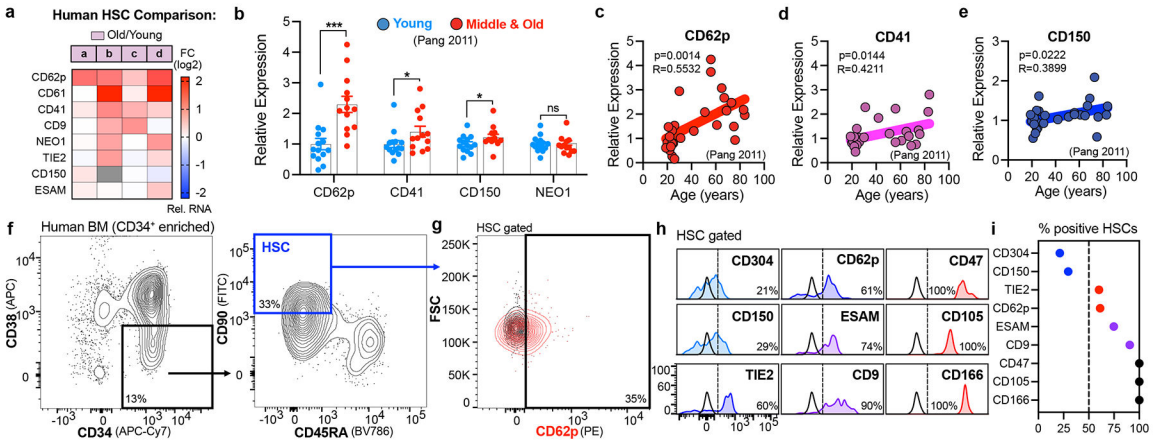

Figure 5 | Mouse myeloid-biased HSC markers are enriched in aged human HSCs

a, Heatmap depicting RNA expression of candidate human my-HSC antigens in independent datasets of human Old vs. Young HSCs (*a*[3], *b*[53], *c*[54], *d*[55]). **b**, Relative RNA expression of CD62p (*Selp*; ***P=0.000211), CD41 (*Itga2b*; *P=0.0325), CD150 (*Slamf1*; *P=0.0359), and NEO1 (*Neo1*; P=0.362) in human HSCs isolated from young (ages 20-31); n=14 donors, middle & old (ages 42-85); n=13 donors; data obtained from Pang[3] (GSE32719). **c–e**, Correlation of relative RNA expression of CD62p (**c**), CD41 (**d**), and CD150 (**e**) in human HSCs compared to donor age; n=27 donors; data obtained from Pang[3] (GSE32719). For **b–e**, values are relative to mean of young samples. **f**, Representative flow-cytometry of CD34$^+$-enriched donor bone-marrow to identify human HSCs (Lin$^-$CD34$^+$CD38$^-$CD45RA$^-$CD90$^+$)[59]. **g**, Representative flow-cytometry staining of HSCs with anti-CD62p antibody (*red*) compared to fluorescence-minus-one (FMO) control (*black*); n=3 independent donors. **h–i**, Histograms for flow-cytometry staining of HSCs with antibodies to CD304, CD150, TIE2, CD62p, ESAM, CD9, CD47, CD105, CD166; black line represents FMO control (**h**), with percent of HSCs positive for each marker (**i**). p-values obtained by unpaired parametric one-tailed t-test (**b**), or p-values and R values calculated with one-tailed Pearson correlation coefficient (**c–e**). FMO, fluorescence-minus-one. Bars indicate mean +/− s.e.m. *P<0.05, **P<0.005, ***P<0.0005; Exact P-values provided in Source Data.